Effects of Radar Beam Shielding on Rainfall Estimation for the Polarimetric C-Band Radar

KATJA FRIEDRICH AND URS GERMANN

MeteoSvizzera, Locarno, Switzerland

JONATHAN J. GOURLEY

National Severe Storms Laboratory, Norman, Oklahoma

PIERRE TABARY

Direction des Systèmes d'Observation, Météo-France, Trappes, France

(Manuscript received 25 July 2006, in final form 5 February 2007)

ABSTRACT

Radar reflectivity (Z_h), differential reflectivity (Z_{dr}), and specific differential phase (K_{dp}) measured from the operational, polarimetric weather radar located in Trappes, France, were used to examine the effects of radar beam shielding on rainfall estimation. The objective of this study is to investigate the degree of immunity of K_{dp}-based rainfall estimates to beam shielding for C-band radar data during four typical rain events encountered in Europe. The rain events include two cold frontal rainbands with average rainfall rates of 7 and 17 mm h^{-1}, respectively, and two summertime convective rain events with average rainfall rates of 11 and 22 mm h^{-1}.

The large effects of beam shielding on rainfall accumulation were observed for algorithms using Z_h and Z_{dr} with differences of up to ~2 dB (40%) compared to a K_{dp}-based algorithm over a power loss range of 0–8 dB. This analysis reveals that Z_{dr} and K_{dp} are not affected by partial beam shielding. Standard reflectivity corrections based on the degree of beam shielding would have overestimated rainfall rates by up to 1.5 dB for less than 40% beam shielding and up to 3 dB for beam shielding less than 75%. The investigation also examined the sensitivity of beam shielding effects on rainfall rate estimation to (i) axis–ratio parameterization and drop size distribution, (ii) methods used to smooth profiles of differential propagation phase (ϕ_{dp}) and estimate K_{dp}, and (iii) event-to-event variability. Although rainfall estimates were sensitive to drop size distribution and axis–ratio parameterization, differences between Z_h- and K_{dp}-based rainfall rates increased independently from those parameters with amount of shielding. Different approaches to smoothing ϕ_{dp} profiles and estimating K_{dp} were examined and showed little impact on results.

1. Introduction

Rainfall estimation by radar is subject to smaller errors when measurements are made at levels close to the ground. The relation between surface rainfall and radar measurements taken at increasing altitudes diminishes due to the vertical variability and horizontal advection of precipitation. Doppler weather radars are typically used for operational rainfall estimation, since they are capable of measuring three-dimensional reflectivity, Doppler velocity, and spectrum width with a spatial resolution of hundreds of meters and temporal resolution within minutes. However, radar data observed at low altitudes are often contaminated by returns from mountains, ocean waves, buildings, or vegetation. Numerous techniques have been developed to detect and remove ground clutter returns based on texture of reflectivity, Doppler spectrum, and clutter maps (Doviak and Zrnić 1993; Joss and Lee 1995; Germann and Joss 2003; Kessinger et al. 2003). Usually the orographic environment around the radar is characterized in terms of calculating the area that is illuminated by the radar beam for a given scanning strategy and radar charac-

Corresponding author address: Dr. Katja Friedrich, MeteoSvizzera, Via ai Monti 146, CH-6605 Locarno Monti, Switzerland. E-mail: katja.friedrich@meteoswiss.ch

DOI: 10.1175/JTECH2085.1

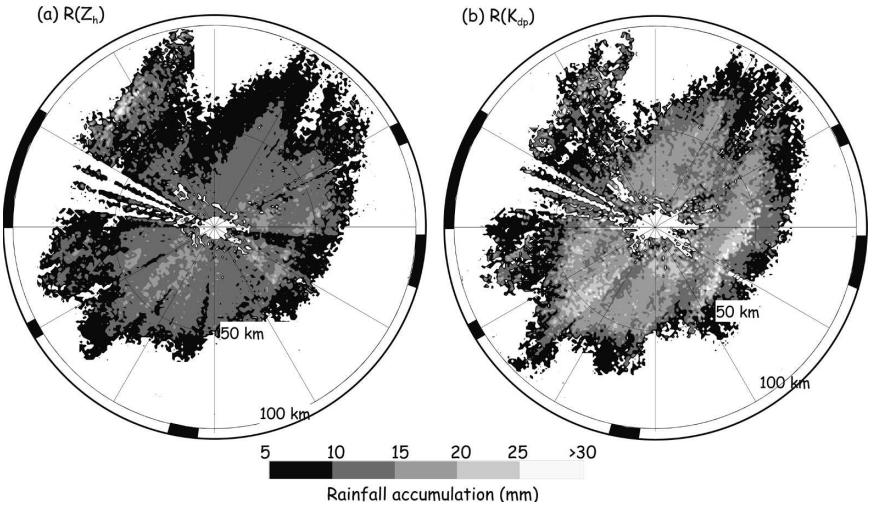

FIG. 1. Six-hour rainfall accumulation (0000–0600 UTC) on 4 Jul 2005 at an 0.4° elevation angle using radar rainfall algorithms based on (a) Z_h denoted as $R(Z_h)$ and (b) K_{dp} denoted as $R(K_{dp})$, respectively. Regions of radar beam shielding >70% are indicated as black-filled semicircle segments located at the outside of the analysis domain. The analysis domain is limited to a range of 5 to 100 km around the Trappes radar located in the center.

teristics. This has been done for most radar sites, especially those located in mountainous terrain (Delrieu et al. 1995; Gabella and Perona 1998; Maddox et al. 2002; Pellarin et al. 2002; Germann et al. 2006). Quantifying and correcting power losses due to beam shielding is especially important for quantitative precipitation estimation in mountainous terrain (Young et al. 1999). Promising results toward this goal based entirely on radar reflectivity and Doppler velocity are shown, for instance, by Andrieu et al. (1997), Creutin et al. (1997), Pellarin et al. (2002), and Germann et al. (2006).

Over the last three decades, potential benefits of polarization diversity for weather radars have also been investigated extensively to improve quantitative precipitation measurements (e.g., Seliga and Bringi 1976; Bringi et al. 1984; Bringi and Hendry 1990; Chandrasekar et al. 1990; Joss and Waldvogel 1990; Gorgucci et al. 1994; Zrnić and Ryzhkov 1999; Illingworth 2003; Szalinska et al. 2005). Polarization diversity allows the transmission and reception of the electric field in different spatial orientations. Polarimetric weather radars are usually limited to transmitting and receiving horizontally and vertically oriented electric fields (also referred to as dual polarization). By combining the differently oriented transmitted and received reflectivities, information about particle size, shape, orientation, and dielectric constant can be obtained. Polarimetric radar variables most commonly derived from dual-polarization measurements are reflectivity at horizontal polarization (Z_h), the ratio of horizontal to vertical reflectivity or differential reflectivity (Z_{dr}), correlation between horizontally and vertically polarized return signals denoted as a correlation coefficient (ρ_{hv}), the phase difference between horizontally and vertically polarized returns or differential propagation phase (ϕ_{dp}), and specific differential phase (K_{dp}) defined as one-half of the range derivative of ϕ_{dp} (Bringi and Chandrasekar 2001).

Rainfall estimates from polarimetric variables are most commonly based either on reflectivity (Z_h, Z_{dr}), K_{dp}, or combinations. Phase measurements have a lower sensitivity to distortions of the amplitude caused by, for example, calibration problems, attenuation, and the presence of hail and are not affected by partial beam shielding (Zrnić and Ryzhkov 1996). Partial beam shielding effects become obvious when comparing reflectivity-based rainfall estimates including Z_h [denoted as $R(Z_h)$] and those based on K_{dp} [denoted as $R(K_{dp})$] as shown in Fig. 1 for a 6-h stratiform rainfall event occurring on 4 July 2005. More information on data processing and a detailed discussion of this case will be given in sections 2 and 4. Although large differences in rainfall accumulation occurred with the different methods, artifacts resulting from radar beam shielding are more evident in the accumulations from the Z_h method. Regions of high beam shielding (>70%) indicated by black-filled semicircle segments correspond to regions of lower $R(Z_h)$ rainfall rates, while $R(K_{dp})$ is hardly affected in those areas. The effect of partial beam shielding for Z_h and K_{dp} is also shown in Fig. 2 as a function of power loss for the same 6-h rainfall event shown in Fig. 1. Median values of Z_h are reduced by

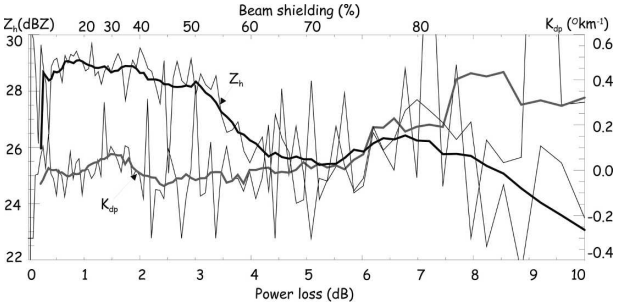

FIG. 2. Same as in Fig. 1, but showing Z_h (black line; scale on the left) and K_{dp} (gray line; scale on the right) as a function of power loss and beam shielding. Medians for each beam shielding class (every 1%) are indicated as thin lines; the centered averaged medians including 10 beam shielding classes are overlaid as thick lines.

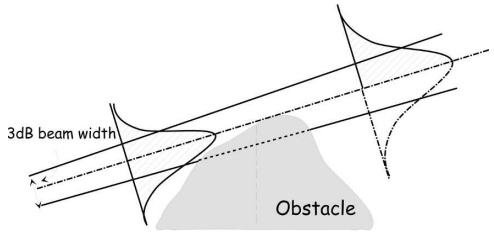

FIG. 3. Two-dimensional schematic illustrating radar beam shielding by an obstacle. The distribution of the transmitted power (hatched area) within the 3-dB beamwidth (black solid lines) is approximated by a Gaussian shape. In this case, 50% of the transmitted radar beam is shielded by the obstacle.

~4 dB for a power loss due to beam shielding of 6 dB. Detailed discussion about the discrepancies will be provided in section 5. This is significant, knowing that the precision in Z_h needed for rainfall rate estimation is approximately 1 dBZ. The polarimetric variables K_{dp} are less affected by beam shielding for losses up to 6 dB. Their median values vary within the experimentally found precision of 0.1° km^{-1} for K_{dp} (Gourley et al. 2006a). Signal-to-noise ratio (SNR) decreases with increasing radar beam shielding, adding an increased uncertainty to phase measurements (Doviak and Zrnić 1993). This might be in effect when more than 70% of the beam is shielded and the variation of K_{dp} increases. In the case of radar beam shielding, a weaker transmitted signal reaches precipitation at further ranges, resulting in a reduced backscattered signal to the receiver as illustrated schematically in Fig. 3. Unbiased phase measurements are possible in these shielded regions where the backscattered signal has been reduced. However, in order to measure small ϕ_{dp} changes in light rain, high accuracy is required. The theoretical standard error of ϕ_{dp}, σ_ϕ, is ~1° primarily related to limits due to the transmission and reception mode (Ryzhkov and Zrnić 1998b; Illingworth 2003). In practice ϕ_{dp} values are contaminated by several factors and σ_ϕ is typically 2°–3° (Hubbert et al. 1993; Ryzhkov and Zrnić 1995; Keenan et al. 1998; Gourley et al. 2006a). Blackman and Illingworth (1993) showed that obstacles cause large, random differential phase shifts. Illingworth (2003) quantifies this phase noise to be ~5° when a random phase is added to precipitation that has a backscatter amplitude 10 times larger. Nevertheless, rain behind obstacles is characterized by small phase fluctuations if the signal-to-noise ratio is sufficiently high.

Several studies focus on the comparison between rainfall estimates using polarimetric variables and surface observations such as rain gauges or disdrometer measurements (see, e.g., Seliga et al. 1981; Aydin et al. 1987, 1995; Gorgucci et al. 1995, 1996; Ryzhkov and Zrnić 1995, 1996; Brandes et al. 1997; Petersen et al. 1999). The potential benefit of polarimetric quantities in mountainous regions was exclusively investigated by Zrnić and Ryzhkov (1996) and Vivekanandan et al. (1999). Zrnić and Ryzhkov (1996) showed an improvement in rainfall rate when the specific differential phase was used in regions where $K_{dp} > 0.4°$ km^{-1} compared to the rainfall rate estimation based on Z_h. The reflectivity during the 2-h period of a mesoscale convective system was on average 6.4 dB lower at 0° compared to the 0.5° elevation angle. After correcting reflectivity for losses due to attenuation and beam shielding using the phase information, Zrnić and Ryzhkov (1996) showed differences in the root-mean-square error between Z_h-based rainfall and gauge data, reducing from 6.8 to 3.6 mm for the lowest elevation. Similar results were achieved during a flash flood event close to Denver, Colorado, investigated by Vivekanandan et al. (1999). They compared rainfall rates derived solely from Z_h and those using K_{dp}. While hardly any differences (~1.4 mm over 4.5 h) occurred in regions with low beam shielding (<40%) differences of 4.7 mm were observed in mountainous terrain with beam shielding of 20%–90% during the same time period.

The objective of this study is to investigate the benefit of K_{dp}-based rainfall estimates as a function of beam shielding for midlatitude precipitation events with average total rainfall amounts of ~5–50 mm using a C-band radar. Reflectivity-based rainfall estimates including Z_h and Z_{dr} [denoted as $R(Z_h)$ and $R(Z_h, Z_{dr})$] are compared to those based on K_{dp} [denoted as $R(K_{dp})$] as a function of beam shielding. Additionally, the influence of beam shielding effects on Z_{dr} are investigated by comparing $R(K_{dp}, Z_{dr})$ to $R(K_{dp})$. Since the comparison of rainfall rates to other instruments (e.g., rain gauges) requires several assumptions and in-

troduces scale mismatches, we will limit this study to an intercomparison of rainfall rates based on polarimetric variables deriving relative differences of rainfall estimates as a function of beam shielding. The studies by Zrnić and Ryzhkov (1996) and Vivekanandan et al. (1999) provided some guidance in addressing this issue, but they are lacking in a few key respects that are important for an operational application in Europe. First, both studies were accomplished with an S-band radar. The differential phase shift ϕ_{dp} consists of two components, the phase difference due to forward scattering and a component related to backscatter differential phase. The latter becomes significant when Mie scattering occurs. While this term is usually negligible at the S band, Mie scattering occurs for raindrops larger than 3 mm for C-band radars ($\lambda \sim 5$ cm). Also, both studies focused on heavy precipitation events causing flash floods. In Vivekanandan et al. (1999) the maximum observed rain amounts accumulated over the entire convective storm event (~4.5 h) was 68 mm, while the squall line observed by Zrnić and Ryzhkov (1996) had maximum accumulated rain amounts of 27 mm over 2 h. This study focuses on more typical rain rates encountered in Europe.

Section 2 describes the observing system and the rainfall characteristics of the four events analyzed in this study. Methodology of the radar processing is explained in section 3. The relation between reflectivity- and K_{dp}-based rainfall accumulations for different amounts of beam shielding is explored in section 4. Special emphasis is placed on the sensitivity to the axis–ratio parameterization and drop size distribution (DSD), the K_{dp} estimation method, and the event-to-event variability. Section 5 discusses the reflectivity correction for beam shielding applied for operational applications. Finally, conclusions are presented in section 6.

2. Observing system, beam shielding map, and event overview

The analysis of rainfall rate estimators is based on data measured by the polarimetric C-band Doppler radar located at Trappes, which is ~30 km southwest of Paris, France. It is operated by the French weather service (Météo-France) and is part of the operational weather radar network (Parent du Châtelet et al. 2005). Transmitted frequency is 5.64 GHz resulting in a wavelength of 5.31 cm. Beamwidth is about 1.1° and pulse width is set to 2 μs. This polarized radar was designed to simultaneously transmit and receive horizontally and vertically polarized waves. It is capable of directly processing Z_h, Z_{dr}, ρ_{hv} at zero time lag, and ϕ_{dp}. Measurements were obtained at an elevation angle of 0.4° every 5 min. Data were collected on a polar coordinate system with a spatial resolution of 0.24 km in range and 0.5° in azimuth. A description of the radar and a detailed examination of the quality of the polarimetric variables were reported in Gourley et al. (2006a).

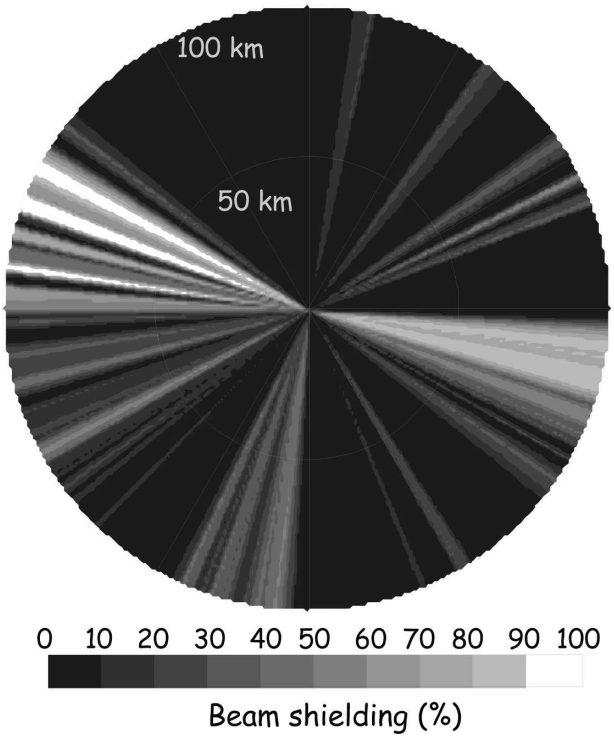

FIG. 4. Horizontal distribution of the amount of beam shielding at an elevation angle of 0.4° around the Trappes radar located in the center.

The impact of beam shielding on reflectivity- and phase-based rainfall rates was analyzed based on the beam shielding map shown in Fig. 4 as a horizontal distribution and in Fig. 5 as a histogram. The beam shielding map reflects the influence of topography and obstacles in the vicinity of the radar (e.g., buildings, trees, and power lines). The effect of topography on radar beam propagation was simulated using the algorithms of Delrieu et al. (1995), a digital terrain model with a horizontal resolution of 250 m, and the Trappes operating characteristics. The Trappes radar is located at an altitude of 191 m MSL with surrounding topography <200 m. At the lowest elevation angle of 0.4° beam shielding caused by topography was <5%. Most of the beam shielding results from urban obstacles located in the vicinity (<5 km) of the radar. Data within the 5-km range are excluded from the analysis. No beam shielding caused by urban obstacles can be assumed beyond the 30-km range. The amount of shield-

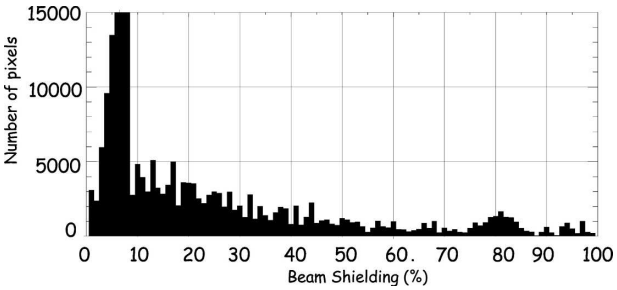

FIG. 5. Histogram of the amount of beam shielding shown in Fig. 4. The amount of beam shielding is divided into 100 classes ranging from 0%–1% to 99%–100% shielding of the radar beam. For clarity of display, the number of pixels is limited to 1.5×10^4. The beam shielding classes 6%–7%, 7%–8%, and 8%–9% include 5.09×10^4, 5.15×10^4, and 1.91×10^4 pixels, respectively.

ing by obstacles was estimated from rainfall accumulated over 14 episodes at farther ranges (60–100 km) because the power losses are evident beyond the ranges where the initial shielding occurred. This range was chosen because data were not affected by contamination due to direct ground clutter and the melting layer during those episodes. Local minima in the accumulated rainfall along the azimuth are related to beam shielding effects, and the amount of shielding was derived as the relative differences between the minimum and the average rainfall accumulation. This method enables the derivation of the total amount of beam shielding for far ranges caused by nearby obstacles, which is then applied to the entire ranges between 5 and 100 km. Resolving the amount of shielding for individual obstacles at certain ranges is difficult. In summary, we assume that the obstacles that cause the discontinuities in the rainfall accumulations are all next to the antenna. It is thus plausible that the true beam shielding at short ranges (5–30 km) is partially overestimated. Finally, beam shielding maps reflecting the influence of topography and urban obstacles are combined (Fig. 4).

The analysis was completed by using four rain events with different precipitation characteristics. Duration of the event and rainfall characteristics based on radar reflectivity measurements over the entire rain period are listed in Table 1; average and maximum rainfall rates were derived from rain gauge measurements within the 100-km radius around Trappes. Two cold frontal rainbands were included in the analysis with average rainfall rates of 7 mm h^{-1} on 17 December 2004 and 17 mm h^{-1} on 4 July 2005. Maximum rainfall rates were 13 mm h^{-1} on 17 December and 37 mm h^{-1} on 4 July. Although the rain on 17 December had the widest spatial extent of the four cases, only ~32% of that area had rainfall rates >20 mm h^{-1}. On 4 July large parts within the observational domain (78.3%) had rainfall rates of >20 mm h^{-1}. Stratiform precipitation occurred on 28 July 2005 with maximum and average rainfall rates of 32.4 and 5.1 mm h^{-1}, respectively. The rain occurred only over 4 h and covered 0.14×10^{-4} km^2 with 20% of the area having rainfall rates larger than 20 mm h^{-1}. Convection was embedded in the stratiform precipitation on 23 June with maximum and average rainfall rates of 51 and 11 mm h^{-1}. In the latter case only 0.52×10^{-4} km^2 were covered by precipitation, while 67% had rainfall rates larger than 20 mm h^{-1}.

3. Data processing

The investigation area was limited to ranges between 5 and 100 km from the radar in order to ensure a superior accuracy of the derived polarimetric variables. Data processing consists of four parts, as schematically illustrated in Fig. 6. First, effects of noise, miscalibration, near-radome interference, and system offset in initial ϕ_{dp} measurements were removed or corrected (Gourley et al. 2006a). Then, echoes primarily related to ground clutter returns from fixed obstacles or due to anomalous propagation, chaff, and scatterers in optical clear air (i.e., insects) were removed using a fuzzy logic algorithm (Gourley et al. 2006b).

For rainfall estimation a more useful parameter than ϕ_{dp} itself is one-half of the range derivative of the two-way differential propagation phase defined as the specific propagation phase K_{dp}. The appendix gives a detailed description about the methodology applied in this analysis for estimating and evaluating K_{dp}. Pixels containing hydrometeor types other than raindrops (e.g., hail, melting snow, and snow) and those that had

TABLE 1. Characteristics of the four analyzed rain events based on radar data: start time, event duration, number of scans included in the analysis, and spatial extent of precipitation averaged over the whole event (accumulated number of pixels per scan where $Z_h >$ 10 dBZ) with percentage fraction >1 and >20 mm h^{-1}. A maximum area of 3.14×10^4 km^2 is covered with a range of 100 km.

Date	Start (UTC)	Duration (h)	No. of scans	Extent (10^4 km^2)	Area > 1 mm h^{-1} (%)	Area > 20 mm h^{-1} (%)
17 Dec 2004	0000	6	72	1.65	62.2	32.1
23 Jun 2005	1200	8	96	0.52	83.1	67.1
4 Jul 2005	0000	10	120	1.17	92.1	78.3
28 Jul 2005	1400	4	48	0.14	46.5	25.6

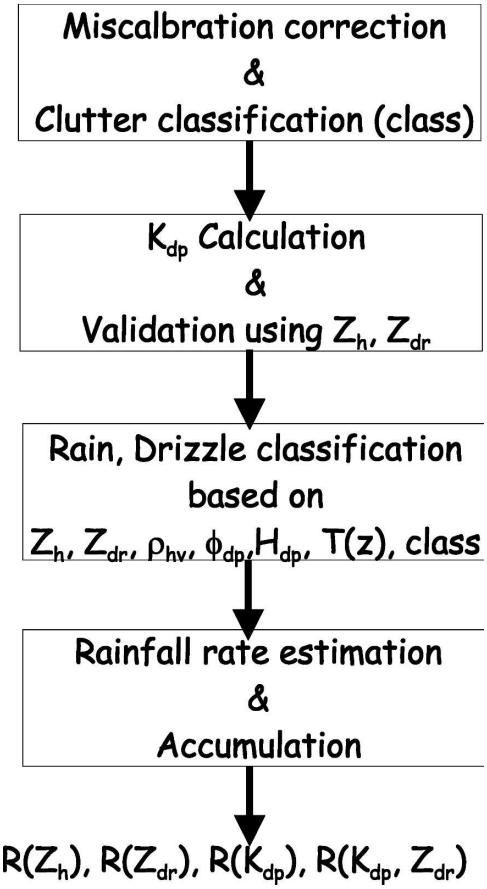

FIG. 6. Schematic showing the different steps of data processing and rainfall accumulation.

reduced Z_h and Z_{dr} values due to attenuation were removed. The applied thresholds are listed in Table 2. Rain and drizzle are primarily identified by combining Z_h, Z_{dr}, and ρ_{hv} measurements. A threshold of $\phi_{dp} < 20°$ was applied to restrict the attenuation of the transmitted power by hydrometeors to <1.4 dBZ for Z_h and <0.4 dB for Z_{dr}. Data containing hail were identified and removed using the differential reflectivity hail signal according to Aydin et al. (1986) originally developed to detect hail for S-band radars. This technique will be applied in this study to C-band radar in the same way as for measurements at S band since Mie resonances occur primarily when $Z_{dr} > 1.75$ dB. Generally, the application of the Aydin technique for C-band radars requires more scrutiny. Also, data observed above and within the melting layer were excluded from the analysis. For every hour, the lower height level of the melting layer was manually identified based on increases in Z_h and reduced values of ρ_{hv}. From the hourly derived lower melting layer heights the overall minimum was derived and data located beyond this range were removed. If the melting layer was not detectable by the radar, the lower height was set 1 km below the 0° isotherm as observed by the Météo-France soundings launched at 0000 and 1200 UTC from Trappes. The melting layer was not intersected within the 100-km range from the radar on 23 June, 4 July, and 28 July 2005, while data beyond the 40-km range for the 0.4° elevation angle were excluded from the analysis on 17 December 2004.

TABLE 2. Thresholds for Z_h, Z_{dr}, and ρ_{hv} used to identify rain and drizzle (based on Keenan 2003). Data were restricted to an approximate attenuation of Z_{dr} of 0.6 dB or smaller and of Z_h of 1.4 dBZ or smaller using the ϕ_{dp} threshold. The differential reflectivity hail signal, H_{dr}, was used to exclude areas containing hail (Aydin et al. 1986).

Polarimetric variable	Threshold for rain and drizzle detection
Z_h	10–60 dBZ
Z_{dr}	0.2–4 dB
ρ_{hv}	>0.97
ϕ_{dp}	<20°
$H_{dr} = Z_h - f(Z_{dr})$	<0
$f(Z_{dr}) = 27$ dB $Z_{dr} \leq 0$ dB	
$f(Z_{dr}) = 27$ dB $+ 19Z_{dr}$ $0 \leq Z_{dr} \leq 1.74$ dB	
$f(Z_{dr}) = 60$ dB $Z_{dr} > 1.74$ dB	

Four radar rainfall algorithms were chosen to estimate rainfall rates based on polarimetric variables. Rainfall rates expressed in units of millimeters per hour were computed at each pixel as

$$R(Z_h) = aZ_h^b, \tag{1}$$

$$R(Z_h, Z_{dr}) = aZ_h^b 10^{cZ_{dr}}, \tag{2}$$

$$R(K_{dp}) = a|K_{dp}|^b \text{sign}(K_{dp}), \tag{3}$$

$$R(K_{dp}, Z_{dr}) = a|K_{dp}|^b 10^{cZdr} \text{sign}(K_{dp}). \tag{4}$$

The units for Z_h are mm^6 m^{-3} and ° km^{-1} for K_{dp}. All relations listed in Eqs. (1)–(4) depend on the relation between shape and size of the drops (denoted as the axis–ratio relation) and assumed drop size distribution. The analysis of disdrometer data collected during three months of convective and stratiform precipitation in a region close to Trappes revealed a mean Z–R relationship of $Z_h = 282\ R(Z_h)^{1.66}$ [corresponding to $a = 0.0334$ and $b = 0.6024$ in Eq. (1)], which is used for operational rainfall rate estimation (Testud 2003). Since the same disdrometer data have not been analyzed for polarimetric rainfall rate quantities, we used theoretical and experimental studies focused on the parameterization of different drop size distributions. Hagen (2001) applied three axis–ratio parameteriza-

TABLE 3. Rainfall rate equations for different DSDs and axis–ratio parameterizations after Hagen (2001). DSDs were based on disdrometer data measured at Oberpfaffenhofen between April and November 1996 and Locarno between September and November 1999; and data based on a simulation. Axis–ratio parameterizations from Pruppacher and Beard (1970), Keenan et al. (1997), and Andsager et al. (1999) were applied to the DSDs in order to calculate values of *a*, *b*, and *c* using a T-matrix scattering program. The text set in boldface highlights the rainfall rate equations used for the analysis beyond section 4b.

Rainfall rate equation for different DSDs	Axis–ratio parameterization from		
	Pruppacher and Beard (1970)	Keenan et al. (1997)	Andsager et al. (1999)
	Oberpfaffenhofen, Germany (48.08°N, 11.28°E), April–November 1996		
$R(Z_h, Z_{dr}) = aZ_h^b 10^{cZdr}$	$\mathbf{a = 0.0221}$	$\mathbf{a = 0.0239}$	$\mathbf{a = 0.0221}$
	$\mathbf{b = 0.82}$	$\mathbf{b = 0.75}$	$\mathbf{b = 0.76}$
	$\mathbf{c = -0.45}$	$\mathbf{c = -0.40}$	$\mathbf{c = -0.33}$
$R(K_{dp}) = a\lvert K_{dp}\rvert^b \operatorname{sign}(K_{dp})$	$\mathbf{a = 18.40}$	$\mathbf{a = 29.08}$	$\mathbf{a = 24.87}$
	$\mathbf{b = 0.79}$	$\mathbf{b = 0.79}$	$\mathbf{b = 0.74}$
$R(K_{dp}, Z_{dr}) = a\lvert K_{dp}\rvert^b 10^{cZdr} \operatorname{sign}(K_{dp})$	$\mathbf{a = 42.73}$	$\mathbf{a = 63.90}$	$\mathbf{a = 57.38}$
	$\mathbf{b = 0.94}$	$\mathbf{b = 0.94}$	$\mathbf{b = 0.90}$
	$\mathbf{c = -0.22}$	$\mathbf{c = -0.25}$	$\mathbf{c = -0.22}$
	Locarno, Switzerland (46.17°N, 8.88°E), September–November 1999		
$R(Z_h, Z_{dr}) = aZ_h^b 10^{cZdr}$	$a = 0.0245$	$a = 0.025$	$a = 0.0215$
	$b = 0.81$	$b = 0.76$	$b = 0.77$
	$c = -0.40$	$c = -0.36$	$c = -0.3$
$R(K_{dp}) = a\lvert K_{dp}\rvert^b \operatorname{sign}(K_{dp})$	$a = 19.66$	$a = 28.81$	$a = 24.92$
	$b = 0.78$	$b = 0.77$	$b = 0.71$
$R(K_{dp}, Z_{dr}) = a\lvert K_{dp}\rvert^b 10^{cZdr} \operatorname{sign}(K_{dp})$	$a = 41.27$	$a = 58.54$	$a = 52.16$
	$b = 0.92$	$b = 0.91$	$b = 0.86$
	$c = -0.2$	$c = -0.23$	$c = -0.2$
	Simulated DSD		
$R(Z_h, Z_{dr}) = aZ_h^b 10^{cZdr}$	$a = 0.0185$	$a = 0.0179$	$a = 0.0172$
	$b = 0.84$	$b = 0.82$	$b = 0.82$
	$c = -0.31$	$c = -0.3$	$c = -0.26$
$R(K_{dp}) = a\lvert K_{dp}\rvert^b \operatorname{sign}(K_{dp})$	$a = 25.81$	$a = 39.06$	$a = 37.14$
	$b = 0.84$	$b = 0.82$	$b = 0.78$
$R(K_{dp}, Z_{dr}) = a\lvert K_{dp}\rvert^b 10^{cZdr} \operatorname{sign}(K_{dp})$	$a = 38.27$	$a = 61.05$	$a = 58.28$
	$b = 0.92$	$b = 0.92$	$b = 0.88$
	$c = -0.13$	$c = -0.19$	$c = -0.17$

tions (Pruppacher and Beard 1970; Keenan et al. 1997; Andsager et al. 1999), two measured and one simulated drop size distribution, to a T-matrix scattering program (Bringi and Chandrasekar 2001) in order to derive the parameters *a, b,* and *c,* in Eqs. (2)–(4) for C-band radar measurements. Table 3 lists nine combinations of parameter settings describing different axis–ratio relations and drop size distributions. Different parameter settings were used in order to investigate the sensitivity of our results to these parameterizations. The results will be discussed in section 4a. The Trappes radar performed a volume scan every 5 min resulting in 12 radar rainfall rate estimates per hour. An hourly rainfall rate on a pixel-by-pixel basis was derived by averaging the scans accomplished every 5 min over one hour. Because of rain advection into and out of the observing domain and the stringent quality control measures, 12 rainfall rate values were not always available per hour. In these cases a minimum number of six values was required to calculate an hourly rainfall rate. Then, the hourly rainfall rate was accumulated over the duration of the rain event, which varied between 4 h for 28 July to 10 h for 4 July 2005 (Table 1).

The following analysis is based on comparing reflectivity- to K_{dp}-based rainfall rates accumulated over the rainfall event. The reflectivity-based rainfall accumulates, $R(Z_h)$ and $R(Z_h, Z_{dr})$, were normalized by $R(K_{dp})$ since $R(K_{dp})$ is considered as the reference rainfall rate immune to beam shielding effects in this analysis. Because nonuniform beam filling effects and low rainfall rates may result in negative values of $R(K_{dp})$ and $R(K_{dp}, Z_{dr})$ [see Eqs. (3)–(4)], negative rain rates are unrealistic and are thus excluded from further analysis. Additionally, the ratio of $[R(K_{dp}, Z_{dr})/R(K_{dp})]$ was analyzed to investigate explicitly the behavior of Z_{dr} with increasing beam shielding. All three relations were expressed in decibels denoted as $10\log_{10}[R(Z_h)/R(K_{dp})]$, $10\log_{10}[R(Z_h, Z_{dr})/R(K_{dp})]$, and $10\log_{10}[R(K_{dp}, Z_{dr})/R(K_{dp})]$. The amount of beam shielding was divided into 100 classes ranging from low beam shielding (0%–

TABLE 4. Characteristics of the statistical significance test for each rainfall event. Total number of hourly accumulated rainfall rate pixels (N_t) and the number of pixels within the high beam shielding dataset ranging between 70% and 100% beam shielding (N_{ds}). Since the number of pixels within a beam shielding class decrease strongly with increasing beam shielding (Fig. 5), fewer beam shielding classes were combined for the low beam shielding dataset. Note that both the low and high beam shielding dataset have the same number of pixels (N_{ds}).

	N_t	N_{ds}	Classes included in the low beam shielding dataset (%)
17 Dec 2004	20 641	1445	0–4
23 Jun 2005	65 170	4563	0–5
4 Jul 2005	39 141	2740	0–5
28 Jul 2005	199 103	9955	0–4

1%) to almost complete beam shielding (99%–100%). Median and variance were derived from a probability density functions of $10\log_{10}[R(Z_h)/R(K_{dp})]$, $10\log_{10}[R(Z_h, Z_{dr})/R(K_{dp})]$, and $10\log_{10}[R(K_{dp}, Z_{dr})/R(K_{dp})]$, which were obtained for each beam shielding class. For simplicity, we will refer to this as the median and variance of $10\log_{10}[R(Z_h)/R(K_{dp})]$, $10\log_{10}[R(Z_h, Z_{dr})/R(K_{dp})]$, and $10\log_{10}[R(K_{dp}, Z_{dr})/R(K_{dp})]$ in the following discussion. For clarity of presentation, the medians were smoothed using a centered moving average technique consisting of 10 beam shielding classes. Results are shown up to a power loss of 10 dB (90% beam shielding). Beyond this power loss the sample sizes become small and the computed medians are noisy.

4. Relation between reflectivity- and K_{dp}-based rainfall accumulations

First, we tested whether the median of the reflectivity- to K_{dp}-based rainfall accumulation within low beam shielding (denoted as μ_l) was significantly different from those obtained within highly shielded areas (denoted as μ_h) using the resampling technique reported in Gourley and Vieux (2005). For each rainfall event, two datasets were created that have the same number of pixels either distributed close to 0% or 100% representing low and high beam shielding, respectively. Table 4 lists the number of pixels and the classes included in the low and high shielding dataset for each rainfall event. Since the number of pixels per class was much higher for low compared to high beam shielding (Fig. 5), the classes for low shielding ranged mainly only from 0% to 5%, while high beam shielding covered 30 classes ranging from 70% to 100%.

The results of the statistical significance test are listed in Table 5. The medians of $10\log_{10}[R(Z_h)/R(K_{dp})]$ and $10\log_{10}[R(Z_{dr}, Z_h)/K(_{dp})]$ were higher in low beam shielding regions ($\mu_l > \mu_h$) in all four analyzed events with differences ($\mu_l - \mu_h$) of 1.77–3.21 dB. The median of $10\log_{10}[R(K_{dp}, Z_{dr})/R(K_{dp})]$ in the low beam shielding area exceeded the median in the high beam shielding region only on 4 July. Differences in the median of $10\log_{10}[R(K_{dp}, Z_{dr})/R(K_{dp})]$ ranged between −0.12 and 0.15 dB. To determine whether the differences between the low and high shielding dataset are significant, the low and high shielding datasets for each rainfall event were combined and randomly separated into two datasets. The median difference for each rainfall event was then computed. This resampling test was performed 1000 times in order to calculate the probability density function of differences due to random chance. The reduction in accumulations for the $R(Z_h)$ and $R(Z_{dr}, Z_h)$ algorithms between low and high shielding regions is statistically significant at the 99% level for all four cases (Table 5). Rain rates from the $R(K_{dp}, Z_{dr})$ algorithm, however, do not decrease with increasing beam shielding at the 99% significance level.

a. Sensitivity to axis–ratio parameterization and drop size distribution

First, the sensitivity of reflectivity- and K_{dp}-based rainfall accumulations on drop size distribution and axis–ratio parameterization was investigated. For each rainfall event (Table 1) the hourly rainfall rate was computed for all nine combinations listed in Table 3 and then accumulated over the event. Figure 7 shows medians of $10\log_{10}[R(Z_h)/R(K_{dp})]$, $10\log_{10}[R(Z_h, Z_{dr})/R(K_{dp})]$, and $10\log_{10}[R(K_{dp}, Z_{dr})/R(K_{dp})]$ for different DSD and axis–ratio parameterizations as a function of the amount of beam shielding for the 4 July case. Although the different DSD and axis ratio parameterizations produced similar trends with increasing beam shielding, large differences of up to ~2 dB for the median of $10\log_{10}[R(Z_h)/R(K_{dp})]$ in Fig. 7a and of ~4 dB for the median of $10\log_{10}[R(Z_h, Z_{dr})/R(K_{dp})]$ in Fig. 7b were observed between the nine combinations. These differences are primarily related to the fact that $R(Z_h)$ was derived from a fixed drop size distribution and axis–ratio parameterization that was found for the Trappes radar (see Testud 2003), while the DSD and axis–ratio parameterizations were varied for $R(Z_h, Z_{dr})$ and $R(K_{dp})$ according to Hagen (2001). The focus of this paper is on the behavior of reflectivity- versus K_{dp}-based rainfall rates as a function of beam shielding and not differences due to different parameterizations.

In Figs. 7a and 7b, the medians of $10\log_{10}[R(Z_h)/R(K_{dp})]$ and $10\log_{10}[R(Z_h, Z_{dr})/R(K_{dp})]$ decreased at a rate of ~0.2 and ~0.3 for power losses (beam shielding) of 0–6 dB (0%–75%), respectively. In particular, the medians of $10\log_{10}[R(Z_h)/R(K_{dp})]$ declined at a rate of 0.2 between 0- and 1.5-dB, 0.4 between 1.5- and 2.8-dB,

TABLE 5. Results of the statistical significance test between one sample that includes data with low beam shielding and a second sample that covers high beam shielding. Differences between the median of the low and high shielding dataset ($\mu_l - \mu_h$), the median of high beam shielding dataset (μ_h), and the 1st and 99th percentiles of the probability density function including the resampled differences are shown. For resampling, data from both datasets were randomly selected and the differences between the medians were calculated. The percentiles were derived from the resampled median differences.

	$\mu_l - \mu_h$ (dB)	μ_h (dB)	1st percentile (dB)	99th percentile (dB)
		17 Dec 2004		
$10\log_{10}[R(Z_h)/R(K_{dp})]$	1.77	−1.74	−0.31	0.30
$10\log_{10}[R(Z_h, Z_{dr})/R(K_{dp})]$	2.10	−2.56	−0.33	0.32
$10\log_{10}[R(K_{dp}, Z_{dr})/R(K_{dp})]$	−0.03	−0.94	−0.10	0.08
		23 Jun 2005		
$10\log_{10}[R(Z_h)/R(K_{dp})]$	2.34	−3.48	−0.14	0.12
$10\log_{10}[R(Z_h, Z_{dr})/R(K_{dp})]$	2.67	−4.42	−0.16	0.13
$10\log_{10}[R(K_{dp}, Z_{dr})/R(K_{dp})]$	−0.12	−1.22	−0.04	0.02
		4 Jul 2005		
$10\log_{10}[R(Z_h)/R(K_{dp})]$	2.51	−3.58	−0.11	0.09
$10\log_{10}[R(Z_h, Z_{dr})/R(K_{dp})]$	3.21	−4.99	−0.13	0.10
$10\log_{10}[R(K_{dp}, Z_{dr})/R(K_{dp})]$	0.15	−1.41	−0.03	0.01
		28 Jul 2005		
$10\log_{10}[R(Z_h)/R(K_{dp})]$	2.14	−4.75	−0.18	0.16
$10\log_{10}[R(Z_h, Z_{dr})/R(K_{dp})]$	2.70	−5.38	−0.22	0.19
$10\log_{10}[R(K_{dp}, Z_{dr})/R(K_{dp})]$	−0.09	−0.75	−0.06	0.04

and 0.3 between 2.8- and 6-dB power loss. The decline rate for the median of $10\log_{10}[R(Z_h, Z_{dr})/R(K_{dp})]$ with increasing beam shielding was slightly higher with 0.3 between 0- and 1.5-dB, 0.5 between 1.5- and 2.8-dB, and 0.4 between 2.8- and 6-dB power loss. Note the centered moving averages (thick lines in Fig. 7) including 10 beam shielding classes were highly influenced by the data included in >8-dB power loss. This effect caused a stagnation and slight increase of the moving average curves between 7 and 10 dB. The number of samples was significantly smaller (<100 pixels per class) beyond 85% beam shielding (Fig. 5), and the medians show strong variation. Since the results beyond 8-dB power loss become questionable, they were not analyzed further in this section. Although the different curves in Figs. 7a and 7b show an offset in the median values, medians of $10\log_{10}[R(Z_h)/R(K_{dp})]$ and $10\log_{10}[R(Z_h, Z_{dr})/R(K_{dp})]$ decreased at almost the same rate. This can give a first indication that the Z_{dr} measurements are less sensitive to beam shielding effects. This effect is much better indicated when comparing $10\log_{10}[R(K_{dp}, Z_{dr})/R(K_{dp})]$ in Fig. 7c. Figure 7c indicates that the medians of $10\log_{10}[R(K_{dp}, Z_{dr})/R(K_{dp})]$ scarcely changed (decline <0.01 between 0 and 6 dB) with increasing beam shielding. However, the contribution of Z_{dr} in Eq. (4) is rather small compared to the influence of K_{dp}. In section 5, the influence of beam shielding on the polarimetric quantities will be investigated in more detail. Again, results beyond 8 dB were excluded from the analysis. Similar trends in the medians of $10\log_{10}[R(Z_h)/R(K_{dp})]$, $10\log_{10}[R(Z_h, Z_{dr})/R(K_{dp})]$, and $10\log_{10}[R(K_{dp}, Z_{dr})/R(K_{dp})]$ were observed for the other rain events (figures not shown). Differences in decrease rate between different DSDs and axis–ratio parameterizations were less then 0.03 between 0 and 6 dB. Therefore, a single DSD from Oberpfaffenhofen, Germany, and the Andsager et al. (1999) drop shape parameterization will be used hereafter. While the DSD observed in Locarno, Switzerland, mainly included heavy Mediterranean rain events in autumn, DSD from Oberpfaffenhofen covered a wide range of stratiform and convective rain events similar to those discussed in this paper.

b. Sensitivity to K_{dp} estimation methods

Three methods were applied for estimating K_{dp} and the results were evaluated using a consistency method. The methodology is explained in the appendix. The evaluation of the ϕ_{dp}-based K_{dp} estimation is shown in Fig. 8 as a function of radar reflectivity and K_{dp} estimation based on Z_h and Z_{dr} for the rainfall event on 4 July 2002. The best agreement with the consistency method was found for the centered finite-difference method compared to the regression-based method (Figs. 8a,c, left). Comparing the centered finite-difference method, the ϕ_{dp}-based K_{dp} is closer to the reflectivity-based K_{dp} using centered differences. The same results were observed when comparing with measured reflectivity. The regression-based techniques showed higher variation than the finite-difference

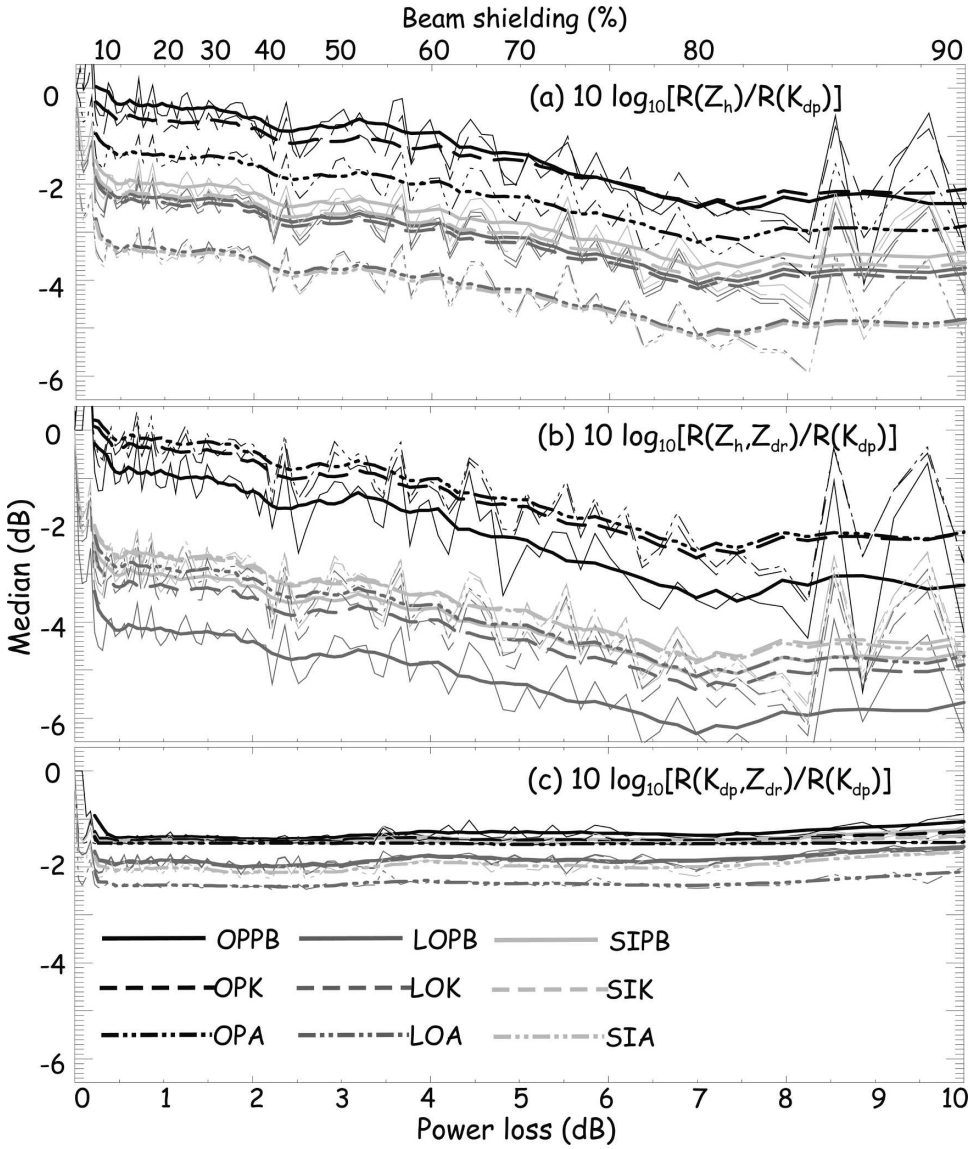

FIG. 7. Median of (a) $10\log_{10}[R(Z_h)/R(K_{dp})]$, (b) $10\log_{10}[R(Z_h, Z_{dr})/R(K_{dp})]$, and (c) $10\log_{10}[R(K_{dp}, Z_{dr})/R(K_{dp})]$ for each shielding class every 1% beam shielding (thin lines) and moving average combining 10 shielding classes (thick lines) for the 6-h rainfall event on 4 Jul 2005. Different gray shading indicates the DSDs. Black lines represent the DSD measured in Oberpfaffenhofen (OP), dark gray lines the DSD measured in Locarno (LO), and light gray lines indicate the simulated DSD (SI). Solid lines indicate axis–ratio parameterization according to Pruppacher and Beard (1970) (PB), dashed lines denote the Keenan et al. (1997) parameterization (K), and dashed–dotted lines represent the Andsager et al. (1999) parameterization (A). The nomenclature of the nine combinations was assembled by the abbreviation of the DSD and axis–ratio parameterization.

methods. Note that the jump in reflectivity at 40 dBZ was caused by the change in averaging interval. The analysis of all cases shows that the K_{dp} method is less sensitive to the smoothing method of ϕ_{dp} profiles but is indeed sensitive to the averaging interval. The analysis in sections 4b and 4c is based on smoothing of the ϕ_{dp} range profiles by a moving average technique and calculating K_{dp} based on centered differences.

Figure 9 shows the median of $10\log_{10}[R(Z_h)/R(K_{dp})]$, $10\log_{10}[R(Z_h, Z_{dr})/R(K_{dp})]$, and $10\log_{10}[R(K_{dp}, Z_{dr})/R(K_{dp})]$ as a function of power loss (beam shielding) for three different methods chosen to estimate K_{dp}. The sensitivity to K_{dp} estimation methods is examined in this section because it has been shown in Ryzhkov and Zrnić (1998a) and Gorgucci et al. (1999) that K_{dp} can be biased either negatively or positively if there is nonuni-

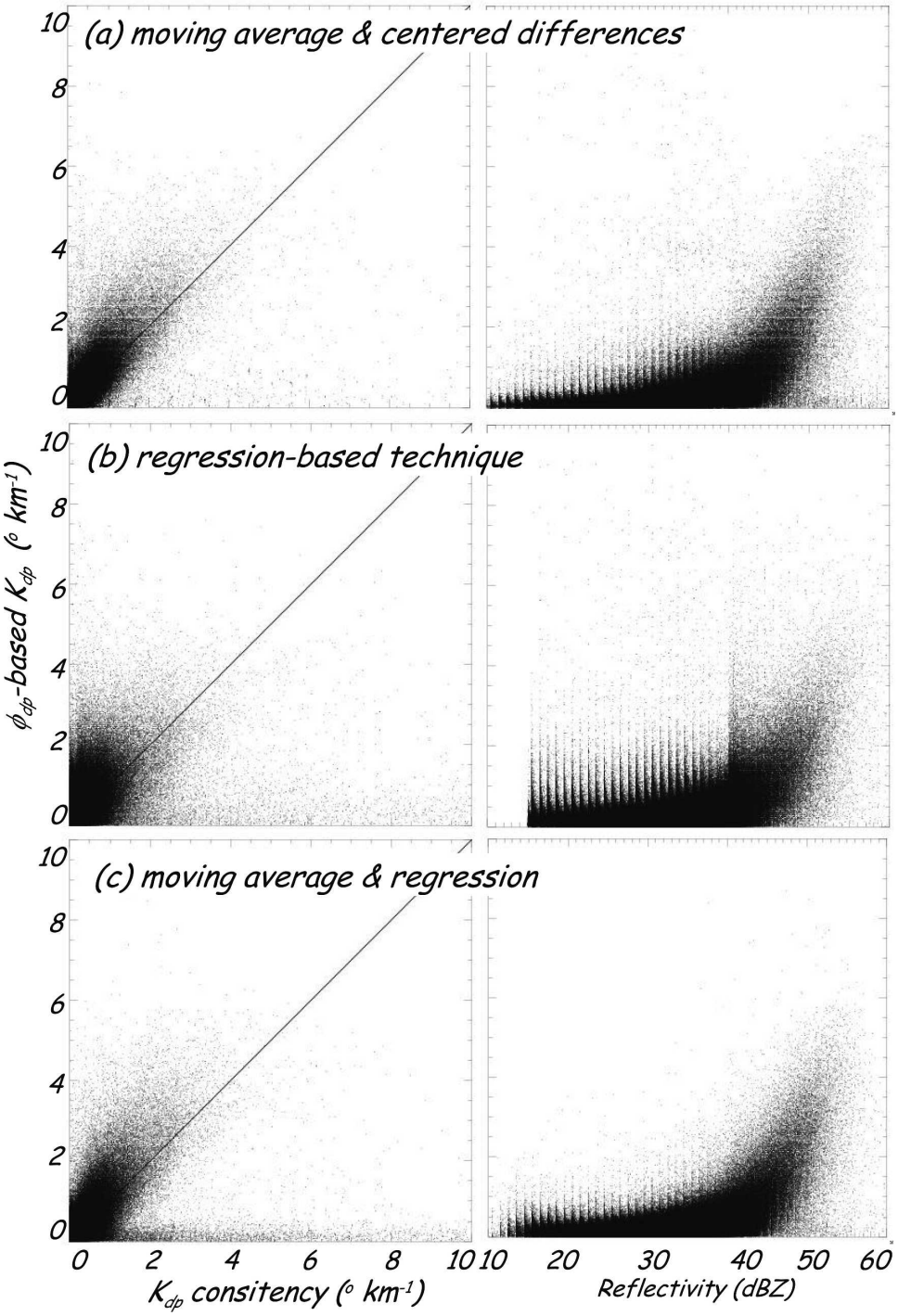

FIG. 8. Scattergrams showing the ϕ_{dp}-based K_{dp} estimations as a function of (left) Z_{dr}–Z_h-based K_{dp} estimations (denoted as K_{dp} consistency) and (right) radar reflectivity during the 6-h rainfall event on 4 Jul 2005. The ϕ_{dp}-based K_{dp} was estimated using (a) a moving average technique to smooth the ϕ_{dp} profiles and a centered-difference approach to calculate K_{dp}, (b) a regression-based technique after Bringi and Chandrasekar (2001), and (c) a moving average technique to smooth the ϕ_{dp} profiles and a regression approach to calculate K_{dp}.

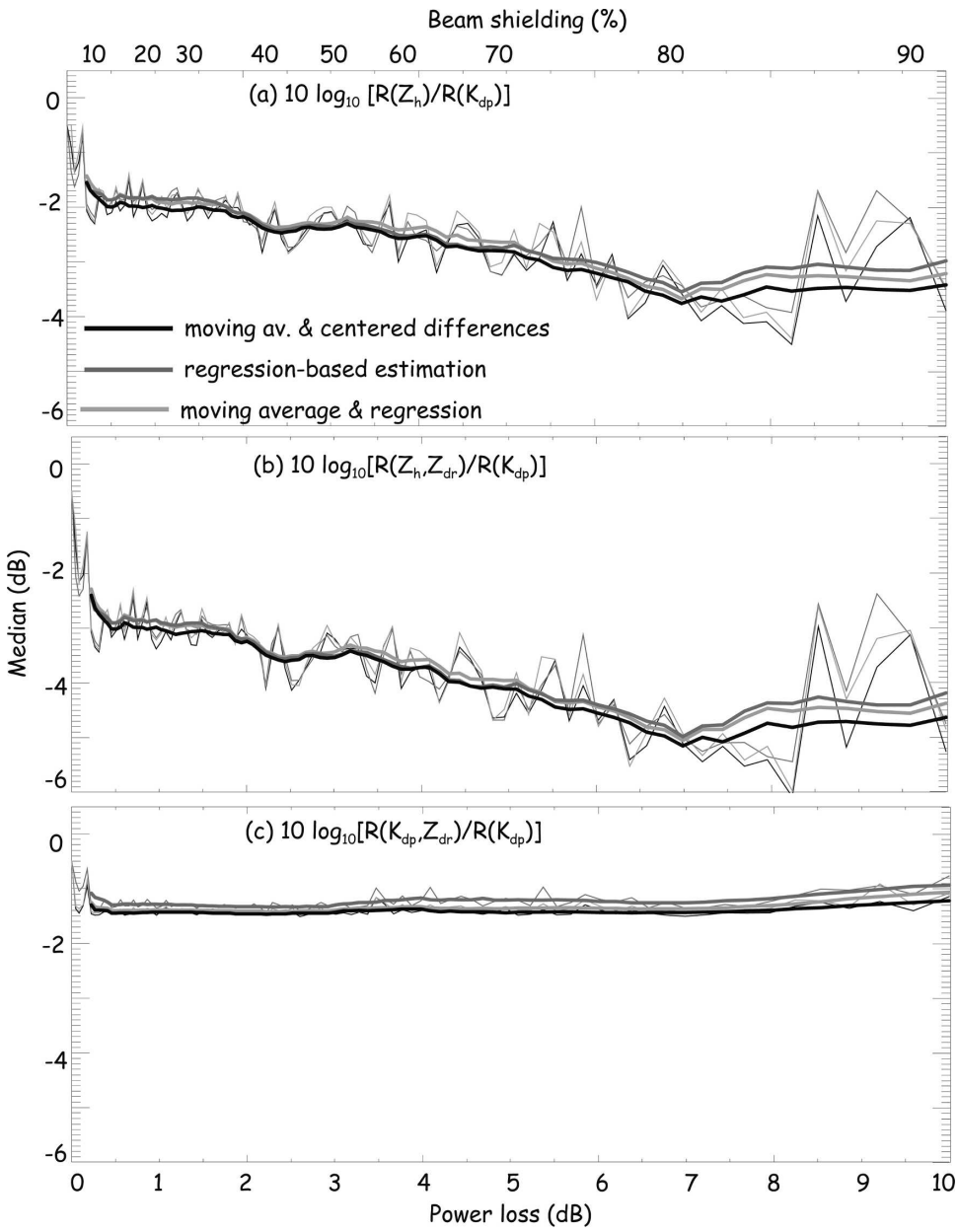

FIG. 9. Same as in Fig. 7, but comparing different techniques to estimate K_{dp} such as the moving average technique to smooth ϕ_{dp} and centered finite differences to estimate K_{dp} (black lines); the regression-based estimate of K_{dp} based on Bringi and Chandrasekar (2001) is indicated by the dark gray lines; and the moving average technique to smooth ϕ_{dp} and a regression method to calculate K_{dp} is indicated by the light gray lines. Rainfall rate equations were based on the DSD measured in Oberpfaffenhofen and the Andsager et al. (1999) axis–ratio parameterizations.

form rainfall in the path over which K_{dp} is estimated and strong azimuthal gradients within the radar resolution volume. Different K_{dp} estimation methods based on regression versus centered finite-difference approaches were tested using data measured on 4 July. The number of pixels included in the analysis varied significantly for the different beam shielding classes (Δbeam shielding = 1%). For more than 50% beam shielding, the number of pixels ranged between 10 and 1000 per class, while for less than 30% the shielding classes contained 1500–50 000 pixels (Fig. 5).

The medians of $10\log_{10}[R(Z_h)/R(K_{dp})]$ and $10\log_{10}[R(Z_{dr}, Z_h)/R(K_{dp})]$ decreased with increasing beam shielding in a similar way for all the three K_{dp}

estimation methods up to 85% beam shielding or 8-dB power loss. The medians declined at a rate of 0.1–0.2 for $10\log_{10}[R(Z_h)/R(K_{dp})]$ and 0.2–0.3 for $10\log_{10}[R(Z_{dr}, Z_h)/R(K_{dp})]$ for all K_{dp} estimation methods between 0- and 6-dB power loss. The decrease of the median was slightly less by ~0.1 for 0–1.5-dB power loss and 0.05 for 1.5–2.8-dB power loss for the regression-based method compared to the finite-difference approach. The differences in the K_{dp} estimation techniques were <0.2 dB for median values of $10\log_{10}[R(K_{dp}, Z_{dr})/R(K_{dp})]$ shown in Fig. 9c with hardly any change with increasing beam shielding. Similar trends were observed for the other rain events (figures not shown). The trend of decreasing $10\log_{10}[R(Z_h)/R(K_{dp})]$ and $10\log_{10}[R(Z_h, Z_{dr})/R(K_{dp})]$ with increasing beam shielding was apparent and independent of the K_{dp} estimation method. The values of $10\log_{10}[R(Z_h)/R(K_{dp})]$, $10\log_{10}[R(Z_h, Z_{dr})/R(K_{dp})]$, and $10\log_{10}[R(K_{dp}, Z_{dr})/R(K_{dp})]$ at a given value of beam shielding are similar for all the K_{dp} estimation methods evaluated in this study. Much higher sensitivities are seen with differences in DSD and axis–ratio parameterizations (see Fig. 7). The following analysis is based on smoothing of the ϕ_{dp} range profiles by a moving average technique and calculating K_{dp} based on centered differences.

c. Event-to-event variability

Figures 10 and 11 show medians and variances of $10\log_{10}[R(Z_h)/R(K_{dp})]$, $10\log_{10}[R(Z_h, Z_{dr})/R(K_{dp})]$, and $10\log_{10}[R(K_{dp}, Z_{dr})/R(K_{dp})]$ for the four rainfall events studied (Table 1). For a direct comparison of the four events, the curves in Fig. 10 were normalized so that their centered average medians at 5% beam shielding (~0.2-dB power loss) are set to 0 dB. Although all curves for $10\log_{10}[R(Z_h)/R(K_{dp})]$ and $10\log_{10}[R(Z_h, Z_{dr})/R(K_{dp})]$ show a decreasing trend with increasing beam shielding at a first glance, the trends were quite different, as indicated by the declining rate for different power loss intervals listed in Table 6. The declining rates for $R(Z_h)$ were derived from the ratio between $10\log_{10}[R(Z_h)/R(K_{dp})]$ and a defined power loss interval. Declining rates for $R(Z_h, Z_{dr})$ were calculated from the ratio between $10\log_{10}[R(Z_h, Z_{dr})/R(K_{dp})]$ and the same power loss interval. The largest decrease of the medians with increasing power loss (0–6 dB) was observed on 4 July and 17 December for the Z_h-based compared to K_{dp} rainfall rate estimates. The decline rates were 0.2 for $R(Z_h)$ and 0.3 for $R(Z_h, Z_{dr})$ for both rainfall events. Smaller decline rates for $R(Z_h)$ and $R(Z_h, Z_{dr})$ were observed during the rainfall events on 23 June and 28 July with values less than or equal to 0.1. Mostly, $R(Z_h, Z_{dr})$ declines at a larger rate compared to $R(Z_h)$, although the maximum always occurs in the same power loss interval, but this interval varied from case to case. The largest decline of $R(Z_h)$ [$R(Z_h, Z_{dr})$] occurred between 0- and 1.5-dB power loss with values of 0.4 [0.5] on 17 December and 0.6 [0.7] on 28 July (Table 6). On 4 July the strongest decline rate with 0.4 for $R(Z_h)$ and 0.5 for $R(Z_h, Z_{dr})$ was found between 1.5- and 2.8-dB power loss. For the rainfall event on 23 June, $R(Z_h)$ and $R(Z_h, Z_{dr})$ decreased strongly during a power loss interval of 2.8–6 dB with values of 0.6 and 0.5, respectively. Interestingly, the decline rates also remained flat, as on 17 December for $R(Z_h, Z_{dr})$. An increase of $R(Z_h)$ and $R(Z_h, Z_{dr})$ with increasing beam shielding was observed on 23 June for a power loss interval of 1.5–2.8-dB power loss and on 28 July of 2.8–6-dB power loss. On 17 December $R(Z_h)$ increased between 2.8- and 6-dB power loss. As a result, an overall decrease of $R(Z_h)$ and $R(Z_h, Z_{dr})$ relative to $R(K_{dp})$ with increasing beam shielding was observed in all cases either through the entire beam shielding range (4 July) or within parts (17 December, 23 June, and 28 July), although variability was noted from case to case. The decrease in median values did not occur as a linear function as expected from the theoretical loss in reflectivity-based rainfall rate, indicated by a thick black line in Figs. 10a,b. This mismatch will be discussed in more detail in section 5. The median of the $10\log_{10}[R(K_{dp}, Z_{dr})/R(K_{dp})]$ curve showed much less sensitivity to beam shielding. The average medians varied by ±0.1 dB between 0- and 3-dB power loss interval for the three summertime cases. The changes in $10\log_{10}[R(K_{dp}, Z_{dr})/R(K_{dp})]$ with increasing beam shielding in Fig. 10c were effectively zero, which indicates that Z_{dr} is not influenced by beam shielding.

The event-to-event variability shows that the largest effects of beam shielding on rainfall estimates relative to $R(K_{dp})$ were observed for $R(Z_h)$ and $R(Z_h, Z_{dr})$, while the smallest effects occurred for $R(K_{dp}, Z_{dr})$. While differences between reflectivity-based and K_{dp}-based rainfall accumulations reached ~−1 dB for power losses (beam shielding) of <2 dB (<40%), differences rose up to −2 dB for higher beam shielding. This result indicates that observed values of Z_h were reduced by beam shielding effects. Curiously, $R(Z_h, Z_{dr})$ was slightly more affected by beam shielding than $R(Z_h)$. Assuming that Z_{dr} values are not biased by beam shielding, the exponent b in estimating $R(Z_h)$ [$b = 0.60$ in Eq. (1)] and $R(Z_h, Z_{dr})$ [$b = 0.76$ in Eq. (2)] causes a higher reduction in $R(Z_h, Z_{dr})$ with Z_h than $R(Z_h)$. For example, a reflectivity loss of 5 dB yields a loss of 3.0 dB for $R(Z_h)$, while a higher loss of 3.8 dB would result for $R(Z_h, Z_{dr})$. This higher theoretical loss for $R(Z_h, Z_{dr})$ compared to $R(Z_h)$ is also indicated in Figs. 10a and 10b. Also, in order to improve rainfall

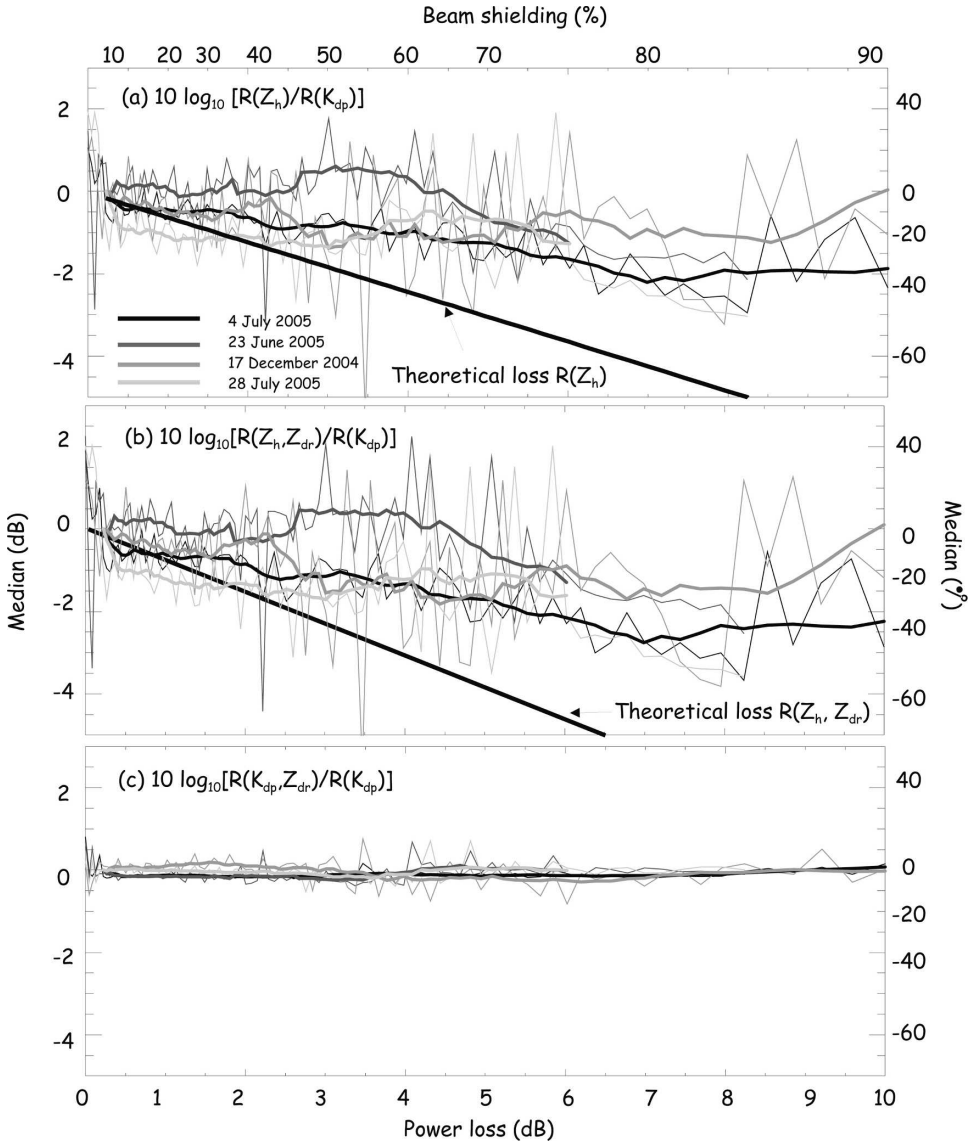

FIG. 10. Same as in Fig. 7, but showing median of (a) $10\log_{10}[R(Z_h)/R(K_{dp})]$, (b) $10\log_{10}[R(Z_h, Z_{dr})/R(K_{dp})]$, and (c) $10\log_{10}[R(K_{dp}, Z_{dr})/R(K_{dp})]$ for rain events measured on 17 Dec 2004 and 23 Jun, 4 Jul, and 28 Jul 2005. Different gray shading indicates the event as shown in (a). The moving average combining 10 beam shielding classes is overlaid (thick lines). For an intercomparison of the cases, the graphs were displaced in a way that the centered moving average medians at 5% beam shielding are located at the zero median. The thick black lines in (a) and (b) indicate the theoretical loss in reflectivity-based rainfall rate to be expected according to the amount of beam shielding. Note that the expected power loss is often used to correct measured reflectivity.

estimations Z_{dr} must be measured within an accuracy of ~0.2 dB. In practice this accuracy may be limited by several factors such as reflectivity gradients and mismatched beams (Illingworth 2003). Because the equations used to derive rain rates are nonlinear and involve multiple polarimetric variables, it is difficult to quantify how Z_{dr} values were impacted by beam shielding using rain rates. The behavior of Z_{dr} with increasing power loss will be discussed in more detail in section 5.

The variance was ~1.5–2 dB for $10\log_{10}[R(Z_h)/R(K_{dp})]$ and $10\log_{10}[R(Z_h, Z_{dr})/R(K_{dp})]$ for the summertime cases, and ~2.2–2.8 dB for the 17 December 2004 case (Fig. 11). A variance of ~0.8 dB was observed for $10\log_{10}[R(K_{dp}, Z_{dr})/R(K_{dp})]$ for all cases. The variation in the median values of all curves increased significantly for beam shielding >80% and <2%. Generally, the number of data points included in the analysis was lower for high (60%–100%) and very

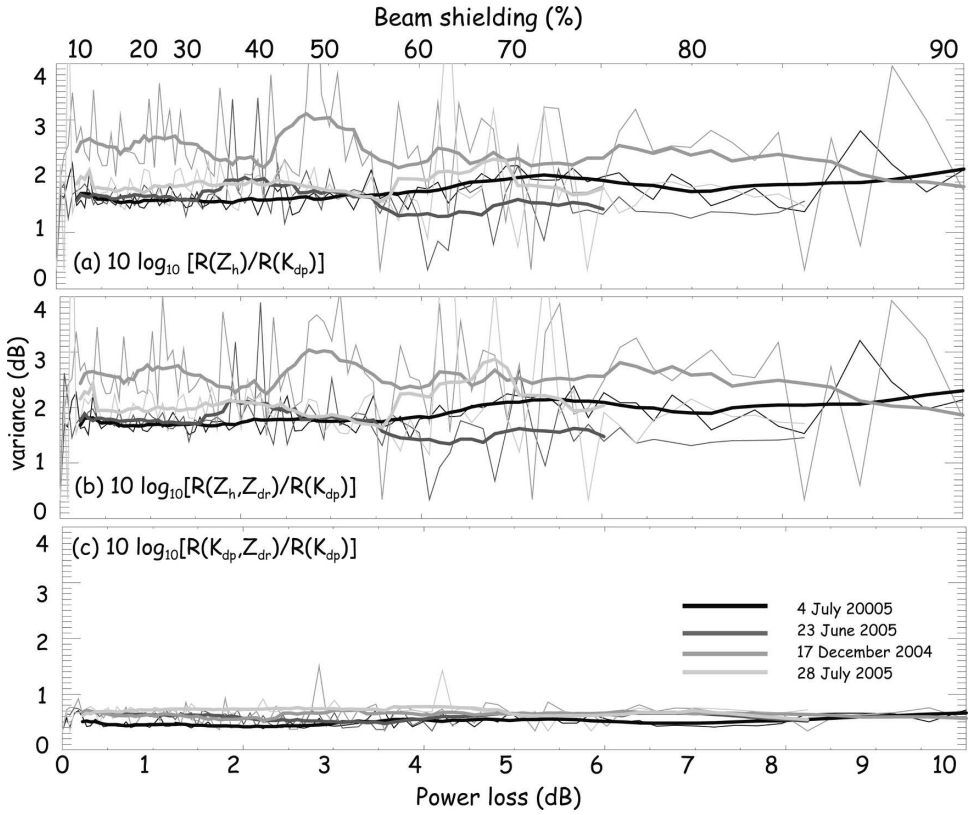

FIG. 11. Variance of (a) $10\log_{10}[R(Z_h)/R(K_{dp})]$, (b) $10\log_{10}[R(Z_h, Z_{dr})/R(K_{dp})]$, and (c) $10\log_{10}[R(K_{dp}, Z_{dr})/R(K_{dp})]$ for rain events measured on 17 Dec 2004 and 23 Jun, 4 Jul, and 28 Jul 2005. The thin lines represent the variances within each shielding class (Δ = 1%); thick lines are the centered moving averages including 10 beam shielding classes.

low (0%–2%) beam shielding compared to 2%–60% beam shielding (Fig. 5). These uncertainties are related either to the reduced number of data points involved in the analysis, inaccuracies in the shielding maps, an inaccurate pointing angle by the radar, or combinations therein. For low and high beam shielding a displacement by only 1° azimuth produces a large impact on the effective beam shielding. This is enforced by the fact that high shielding mainly due to urban obstacles only occurred along isolated rays (Fig. 4). Doviak and Zrnić (1993) also claimed that with a decrease of SNR, phase measurements have an increased uncertainty but no bias. It is plausible that at beam shielding of 80%–100%, the SNR became too low and resulted in noisy $R(K_{dp})$ estimates.

5. Discussion of partial beam shielding effects on K_{dp}, Z_h, and Z_{dr}

The analysis in section 4c is based on the assumption that K_{dp} measurements are not effected by partial beam

TABLE 6. List of declining rates for $R(Z_h)$ and $R(Z_h, Z_{dr})$. The declining rates for $R(Z_h)$ were derived from the ratio between average median of $10\log_{10}[R(Z_h)/R(K_{dp})]$ and a defined power loss interval; the declining rates for $R(Z_h, Z_{dr})$ represent the ratio between $10\log_{10}[R(Z_h, Z_{dr})/R(K_{dp})]$ and a defined power loss interval. Data were fitted to a linear model by minimizing the chi-square error statistic; curves are shown in Figs. 10a,b. Events are sorted according to the ratio for a power loss between 0 and 6 dB.

	$10\log_{10}[R(Z_h)/R(K_{dp})]$ (dB)				$10\log_{10}[R(Z_h, Z_{dr})/R(K_{dp})]$ (dB)			
Power loss interval (dB)	0–1.5	1.5–2.8	2.8–6	0–6	0–1.5	1.5–2.8	2.8–6	0–6
4 Jul 2005	−0.2	−0.4	−0.3	−0.2	−0.3	−0.5	−0.4	−0.3
17 Dec 2004	−0.4	−0.3	0.2	−0.2	−0.5	−0.4	0.0	−0.3
23 Jun 2005	−0.1	0.2	−0.6	−0.1	−0.2	0.3	−0.5	−0.1
28 Jul 2005	−0.6	−0.2	0.1	0.0	−0.7	−0.2	0.1	−0.1

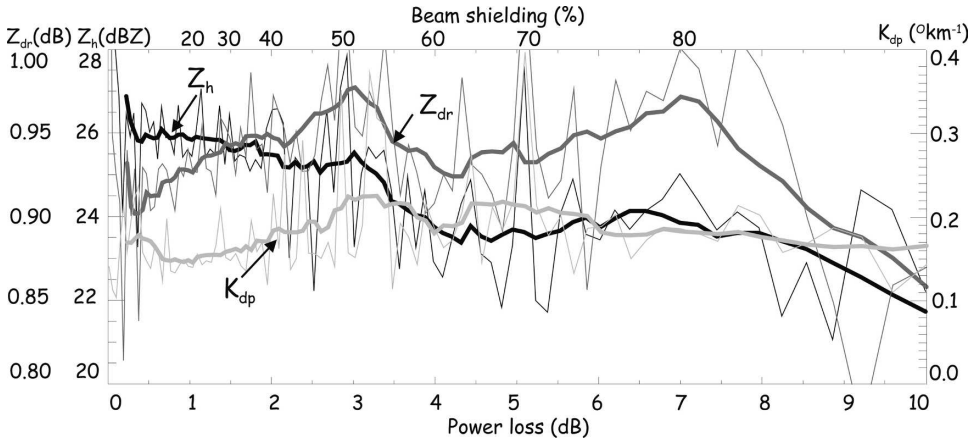

FIG. 12. Mean Z_h (black line; scale on the left), Z_{dr} (dark gray line; scale on the left), and K_{dp} (light gray line; scale on the right) averaged over all four rainfall events as a function of power loss and beam shielding. Mean values for each beam shielding class (every 1%) are indicated as thin lines; the centered averaged means including 10 beam shielding classes are overlaid as thick lines.

shielding. This hypothesis is supported by the average K_{dp} of the four rainfall events shown in Fig. 12. Values of K_{dp} ranged within the experimentally found precision of 0.1° km^{-1} and reveal no dependency on beam shielding. On the contrary, Z_h decreases by ~5 dB for a power loss of 10 dB (Fig. 12), as already indicated for rainfall rates in section 4c. Interestingly, the loss in $R(Z_h)$ is smaller than the theoretical loss in reflectivity-based rainfall rate. This is significant because for an operational application a fast and straightforward approach to correct radar reflectivity for beam shielding effect is conducted by adding the power loss based on the shielding map to the measured reflectivity in decibels. Note that this correction can also be accomplished by converting the power loss in terms of loss in rainfall rate using Eq. (1). In Fig. 10, the estimated power loss based on the Trappes beam shielding map and the theoretical loss of the reflectivity-based rainfall rate [Eq. (1)] is indicated by the thick black line. As an example, 2 dB would need to be added to the measured reflectivity (dB) to compensate for a power loss of 2 dB (37% beam shielding). For the Swiss operational radar located in the Alps, radar reflectivity is corrected for a maximum power loss of 2 dB, and the corrected pixels are weighted according to the visibility (Germann et al. 2006). For the French operational radar rainfall product radar reflectivity is corrected for partial beam shielding up to 5-dB (70%) power loss (Tabary 2007). Figure 13 shows a zoom-in of Fig. 10a for a power loss of 0–2 dB. The average medians on 4 July and 17 De-

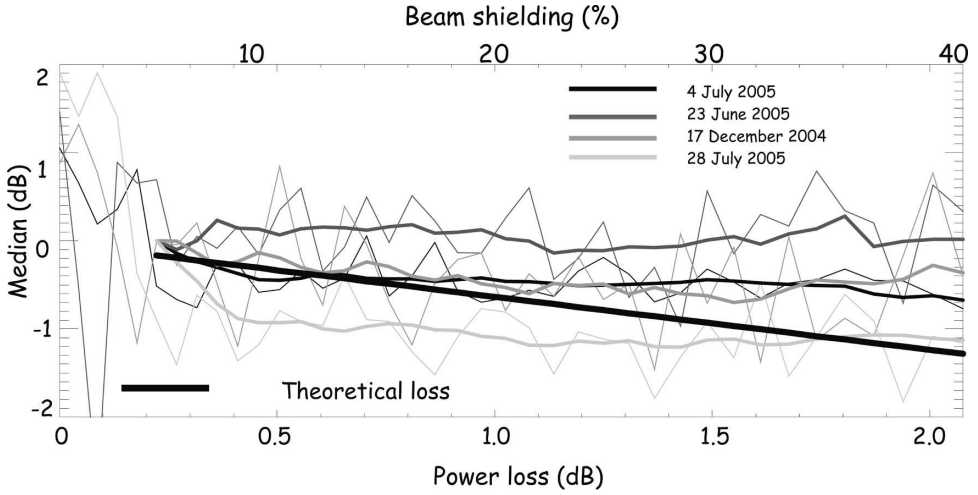

FIG. 13. Same as in Fig. 10a, but zoomed into the power loss region ranging from 0 to 2 dB.

cember agree well (±0.1 dB) with the theoretical assumption between 0- and 1-dB power loss. For power losses between 1 and 2 dB the median values were 0.6 (1.0) dB larger than expected losses for the 4 July (17 December) case. On 23 June, however, the differences were mainly 0.6–1.2 dB. On 28 July median values were up to 0.6 dB lower than the reflectivity correction for low shielding (0–1-dB power loss). With increasing beam shielding the average median approached the reflectivity correction. Figure 11a indicates that the reflectivity correction beyond 2-dB power loss can create biases of up to a factor of 3. Generally, the slopes of the medians with increasing beam shielding for the four cases are much lower than the theoretical value.

The largest uncertainty between measured and theoretical loss in rainfall rate is related to the representativeness of obstacles near the radar in the beam shielding map. As described in section 2, the amount of shielding is overestimated in the vicinity of the radar. Therefore, observed $R(Z_h)$ is larger than expected from the beam shielding map, resulting in a lower decrease of $R(Z_h)/R(K_{dp})$ compared to the theoretical loss. While the total amount of beam shielding for far ranges can be estimated using rainfall accumulations, resolving the amount of shielding for individual obstacles is difficult. As a result, the accuracy of reflectivity correction strongly depends on the accuracy of the beam shielding map. Wrong antenna pointing both in azimuth and elevation can result in significant errors in the correction of $R(Z_h)$ based on a beam shielding map. Further reasons for the mismatch between theoretical and measured $R(Z_h)$ loss remain speculative. Based on rainfall amounts and their distribution (see section 2), a wide variation in drop size distribution can be assumed that might not represent the estimated Z–R relationship. Variability might be related to the differences in DSD, causing the $R(Z_h)$ and $R(Z_h, Z_{dr})$ algorithms to yield different rainfall amounts relative to $R(K_{dp})$. The accuracy of the ϕ_{dp} measurement also influences the results. A lot of emphasis in this study was put on different methods of filtering ϕ_{dp} profiles and deriving K_{dp} measurements. In addition, phase shifts are small at low rainfall rates, which results in noisy ϕ_{dp} measurements. Last, noisy ϕ_{dp} measurements result from small amounts of ground clutter and mismatched sidelobe signals.

The analysis in section 4c reveals another interesting question on whether Z_{dr} is influenced by partial beam shielding. According to Fig. 12, Z_{dr} is not significantly affected by beam shielding. Values range between the experimentally found precision of 0.2 dB and show no dependency on beam shielding effects. Giangrande and Ryzhkov (2005) observed azimuthal modulations of Z_{dr} within uniform precipitation only at the lowest elevation angle of 0.5°. In their cases the Z_{dr} bias was as large as 0.8 dB, which they related to partial beam shielding effects. They associated the origin of the Z_{dr} bias to the mismatch of the antenna beam in the horizontal and vertical polarization, multipath propagation with different characteristics in the vertical and horizontal wave, and effects of semitransparent obstacles such as trees in the vicinity of the radar. The Trappes radar is located on top of a 15-m-high tower to avoid the influence of obstacles nearby the radar. Most of the ground clutter contamination results from urban obstacles occurring within a 25-km range (see Fig. 1 in Gourley et al. 2006b). However, azimuthal modulations can also be caused by radome and near-radome interferences, which were discovered for the Trappes radar by Gourley et al. (2006a). In their case, Z_{dr} varied within a semiregular pattern by ~0.5 dB at an elevation of 1.5°, which is unblocked by obstacles and ground clutter.

6. Conclusions

The influence of radar beam shielding on reflectivity- and K_{dp}-based rainfall estimates hsd been investigated with data obtained by the operational, polarimetric C-band weather radar located in Trappes, France. The behavior of $R(Z_h)$, $R(Z_h, Z_{dr})$, and $R(K_{dp}, Z_{dr})$ with increasing beam shielding with respect to $R(K_{dp})$ was investigated focusing on three main issues: 1) the sensitivity of the results to axis–ratio parameterization and drop size distribution, 2) the sensitivity to K_{dp} estimation methods comparing regression with centered difference approaches, and 3) the representativeness of the results in terms of event-to-event variability. The analysis was based on four typical rain events encountered in Europe including cold frontal rainbands with average rainfall rates of ~7 mm h^{-1} in winter, and one event with average values of ~17 mm h^{-1} in summertime. Also two summertime events were part of the analysis with stratiform precipitation and partially embedded convection with average rainfall rates of 5–11 mm h^{-1}.

Nine combinations of rainfall estimates consisting of three drop size distributions and three axis–ratio parameterizations were assessed (Table 3). Although the rainfall estimates were sensitive to drop size distribution and axis–ratio parameterization, the trends occurring with increasing beam shielding were independent from these parameters. Influences of K_{dp} and fluctuations of ϕ_{dp} were not apparent on the relationship between reflectivity- and K_{dp}-based rainfall accumulation. Rainfall accumulations from K_{dp} were insensitive to three different methods examined to estimate K_{dp} from ϕ_{dp} profiles.

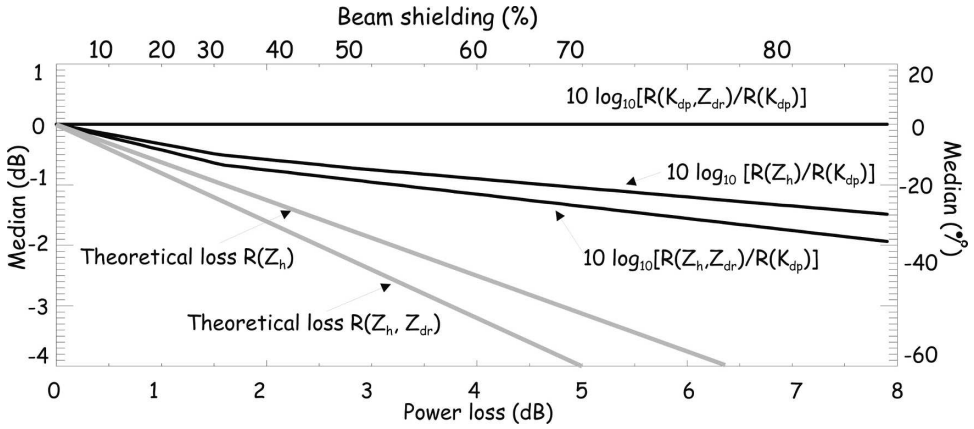

FIG. 14. Schematic diagram summarizing the results of this study. The thick black lines illustrate the behavior of $R(Z_h)$, $R(Z_{dr})$, and $R(K_{dp}, Z_{dr})$ with respect to $R(K_{dp})$. The results are based on four rainfall events with different rainfall characteristics (Table 1). The gray lines indicate the theoretical loss of reflectivity-based rainfall rate according to the power loss from the beam shielding map.

The influence of beam shielding on $R(Z_h)$, $R(Z_h, Z_{dr})$, and $R(K_{dp}, Z_{dr})$ is summarized in Fig. 14. Large effects of beam shielding on rainfall accumulations were observed for $R(Z_h)$ and $R(Z_h, Z_{dr})$ with differences up to ~2 dB (40%) compared to $R(K_{dp})$ over a beam shielding range of 0–8 dB. In two of the four events the strongest decrease in $10\log_{10}[R(Z_h)/R(K_{dp})]$ and $10\log_{10}[R(Z_h, Z_{dr})/R(K_{dp})]$ occurred between 0 and 1.5 dB. Analyzing the behavior of Z_{dr} and K_{dp} with increasing power loss shows that Z_{dr} and K_{dp} are not affected by beam shielding. Mean values range within the experimentally found precision of 0.2 dB for Z_{dr} and 0.1° km^{-1} for K_{dp}. Although Z_{dr} hardly varies with increasing power loss, $R(Z_h, Z_{dr})$ seems to be more affected by beam shielding than $R(Z_h)$. This discrepancy can be related to the difference in the b exponents in Eqs. (1) and (2), which means that $R(Z_h, Z_{dr})$ varies more with Z_h than $R(Z_h)$. Also, rainfall rate estimations using Z_{dr} are more sensitive to accuracy of Z_{dr} than Z–R relationships with respect to Z_h. Interestingly, radar reflectivity (Fig. 2) and reflectivity-based rainfall (Fig. 10) decreased at a lower rate than the reflectivity correction theory. If the reflectivity of the four cases studied would have been corrected for beam shielding effects by adding the power loss, the rainfall rate would have been overestimated by as much as 0.5 dB for power loss <1.5 dB. For higher power losses the rainfall rate would have been overestimated up to ~3 dB. This mismatch between the results and the reflectivity correction is primarily related to the accuracy with which the beam shielding map was derived. While topography is typically known with a high spatial resolution, urban obstacles and trees within less than a 5-km range from the radar are very hard to resolve with beam shielding maps. Only small effects (±0.5 dB) occurred for $R(K_{dp}, Z_{dr})$ compared to $R(K_{dp})$. Large variability in the polarimetric variables occurred for power losses >6 dB (75% beam shielding), increasing significantly for power losses larger than 8 dB (~85% beam shielding).

Acknowledgments. We extend special thanks to Jacques Parent du Châtelet of Météo-France; Gianmario Galli and Bertrand Calpini of MeteoSwiss; Martin Hagen of Deutsches Zentrum für Luft- und Raumfahrt Oberpfaffenhofen; Alexander Ryzhkov of the University of Oklahoma; and the anonymous reviewer for providing comments and suggestions that enhanced the quality of the paper. The authors thank Kim DoKhac of Météo-France for assisting in the acquisition of the radar data. This research is part of the collaboration between Switzerland and France in the INTERREG IIIa project "Radar de Franche-Comté." It is co-funded by the European Union, the French Ministère de l'Ecologie et du Dèveloppment Durable, Météo-France, MeteoSwiss, the Swiss State Secretariat for Economic Affairs, and the Swiss cantons Neuchâtel, Bern, Jura, Basel Landschaft, Fribourg, and Vaud.

APPENDIX

Methodology for Estimating and Evaluating K_{dp}

Several methods have been evaluated to calculate K_{dp} with C-band radars, for example, those of May et al. (1999), Bringi and Chandrasekar (2001), and Testud et al. (2000). Here, K_{dp} is estimated as one-half the range derivative of ϕ_{dp}. Since ϕ_{dp} fluctuates typically

~3°–6°, the accuracy of K_{dp} can be increased by smoothing the range profile. The standard deviation of the K_{dp} estimation depends on the standard deviation of ϕ_{dp} and the selection of the range averaging interval (Bringi and Chandrasekar 2001). Several approaches for K_{dp} estimations have been reported over the last years (e.g., Hubbert et al. 1993; Hubbert and Bringi 1995; Ryzhkov and Zrnić 1996). In this study, two approaches are chosen for estimating K_{dp}, the smoothing of the ϕ_{dp} range profiles (i.e., moving average) and a regression-based estimation.

First, noisy measurements from nonmeteorological echoes were removed by eliminating pixels where the standard deviation of ϕ_{dp} within 10 consecutive range gates was >10° (modified from Ryzhkov and Zrnić 1998b). In this analysis, three K_{dp} estimations were tested: 1) smoothing of the ϕ_{dp} range profiles by a moving average technique and calculating K_{dp} based on centered differences; 2) as in estimation 1, but K_{dp} is derived by calculating the regression within the range averaging interval; and 3) the regression-based estimation of K_{dp} following Bringi and Chandrasekar (2001). Ryzhkov and Zrnić (1996) reveal that at low rain rates the standard deviation of K_{dp} depends strongly on the radial resolution of K_{dp} estimates. They suggest using a heavy filtering (in their case 7–11 km) below a specific radar reflectivity threshold (in their case 40 dBZ) and a light filter (in their case 2–4 km) above this threshold. Their analysis of 15 storms revealed a standard deviation of K_{dp} of 0.12°–0.3° km^{-1} for light filtering and 0.04°–0.10° km^{-1} for heavy filtering. With an error of only 0.1° km^{-1}, K_{dp} has to be at least 1° km^{-1} corresponding to a rainfall rate of ~22 mm h^{-1} for the standard error in rainfall rate for S-band radar to be less than 10%. Two range averaging intervals were chosen according to the reflectivity value (Ryzhkov and Zrnić 1996). Generally, the ϕ_{dp} range profiles are averaged over an interval of 5.8 km (24 consecutive gates). Since large averaging intervals led to an underestimation of K_{dp} for local reflectivity maxima, the averaging interval was reduced to 2 km (8 pixels) when the reflectivity exceeded 40 dBZ.

A technique for radar calibration, developed by Goddard et al. (1994) for a 3-GHz radar, is used to estimate K_{dp} from Z_h and Z_{dr}. It uses a drop size shape model that is based upon empirical adjustments to linear shapes for drops >1.1 mm so that the technique is less sensitive to drop size distribution. A fourth-order polynomial is then fit to the model to ensure a computationally fast application as follows:

$$K_{dp} = 2 \times 10^{-5}(-0.4252Z_{dr}^4 + 3.4683Z_{dr}^3 - 9.8064Z_{dr}^2 + 10.083Z_{dr} + 1.2135)Z_h. \quad \text{(A1)}$$

To reduce the effects of hydrometeor attenuation on Z_h and Z_{dr}, a linear ϕ_{dp}-based method is applied to correct attenuation effects (Bringi et al. 1990) as

$$Z_h(r) = Z'(r)_h + \alpha[\phi_{dp}(r) - \phi_{dp}(0)] \quad \text{(A2)}$$

$$Z_{dr}(r) = Z'_{dr}(r) + \beta[\phi_{dp}(r) - \phi_{dp}(0)], \quad \text{(A3)}$$

where $Z'_h(r)$, $Z'_{dr}(r)$ is the observed reflectivity and differential reflectivity at range r, Z_h and Z_{dr} are the attenuation-corrected values, and $\phi_{dp}(0)$ is the system ϕ_{dp} value. The coefficient α is set to 0.07, and β is 0.02, which represents the mean correction coefficients for C band as derived from several case studies (Carey et al. 2000).

REFERENCES

Andrieu, H., J. D. Creutin, G. Delrieu, and D. Faure, 1997: Use of weather radar for the hydrology of a mountainous area. Part I: Radar measurement interpretation. *J. Hydrol.,* **193,** 1–25.

Andsager, K., K. V. Beard, and N. F. Laird, 1999: Laboratory measurements of axis ratios for large raindrops. *J. Atmos. Sci.,* **56,** 2673–2683.

Aydin, K., T. A. Seliga, and V. Balaji, 1986: Remote sensing of hail with a dual-linear polarization radar. *J. Climate Appl. Meteor.,* **25,** 1475–1484.

——, H. Direskeneli, and T. A. Seliga, 1987: Dual-polarization radar estimation of rainfall parameters compared with ground-based disdrometer measurements: October 29, 1982 Central Illinois experiment. *IEEE Trans. Geosci. Remote Sens.,* **GE-25,** 834–844.

——, V. N. Bringi, and L. Liu, 1995: Rain-rate estimation in the presence of hail using S-band specific differential phase and other radar parameters. *J. Appl. Meteor.,* **34,** 404–410.

Blackman, M., and A. J. Illingworth, 1993: Differential phase measurement of precipitation. Preprints, *26th Conf. on Radar Meteorology,* Norman, OK, Amer. Meteor. Soc., 745–747.

Brandes, E. A., J. Vivekanandan, and J. W. Wilson, 1997: Radar rainfall estimates of the Buffalo Creek flash flood using WRS-88D and polarimetric radar data. Preprints, *28th Conf. on Radar Meteorology,* Austin, TX, Amer. Meteor. Soc., 123–124.

Bringi, V. N., and A. Hendry, 1990: Technology of polarization diversity radar for meteorology. *Radar in Meteorology: Battan Memorial and 40th Anniversary Radar Meteorology Conference,* D. Atlas, Ed., Amer. Meteor. Soc., 153–190.

——, and V. Chandrasekar, 2001: *Polarimetric Doppler Weather Radar: Principles and Applications.* Cambridge University Press, 636 pp.

——, T. A. Seliga, and K. Aydin, 1984: Hail detection with a differential reflectivity radar. *Science,* **225,** 1145–1147.

——, V. Chandrasekar, N. Balakrishnan, and D. S. Zrnić, 1990: An examination of propagation effects in rainfall on radar measurements at microwave frequencies. *J. Atmos. Oceanic Technol.,* **7,** 829–840.

Carey, L. D., S. A. Rutledge, D. A. Ahijevych, and T. D. Keenan, 2000: Correcting propagation effects in C-band polarimetric radar observations of tropical convection using differential propagation phase. *J. Appl. Meteor.,* **39,** 1405–1433.

Chandrasekar, V., V. N. Bringi, N. Balakrishnan, and D. S. Zrnić, 1990: Error structure of multiparameter radar and surface measurements of rainfall. Part III: Specific differential phase. *J. Atmos. Oceanic Technol.,* **7,** 621–629.

Creutin, J. D., H. Andrieu, and D. Faure, 1997: Use of weather radar for the hydrology of a mountainous area. Part II: Radar measurement validation. *J. Hydrol.,* **193,** 26–44.

Delrieu, G., J. Creutin, and H. Andrieu, 1995: Simulation of radar mountain returns using a digitized terrain model. *J. Atmos. Oceanic Technol.,* **12,** 1038–1049.

Doviak, R. J., and D. S. Zrnić, 1993: *Doppler Radar and Weather Observations.* Academic Press, 562 pp.

Gabella, M., and G. Perona, 1998: Simulation of the orographic influence on weather radar using a geometric–optics approach. *J. Atmos. Oceanic Technol.,* **15,** 1485–1494.

Germann, U., and J. Joss, 2003: Operational measurement of precipitation in mountainous terrain. *Weather Radar: Principles and Advanced Applications,* P. Meischner, Ed., Springer-Verlag, 52–77.

——, G. Galli, M. Boscacci, and M. Bolliger, 2006: Radar precipitation measurement in a mountainous region. *Quart. J. Roy. Meteor. Soc.,* **132,** 1669–1692.

Giangrande, S. E., and A. V. Ryzhkov, 2005: Calibration of dual-polarization radar in the presence of partial beam blockage. *J. Atmos. Oceanic Technol.,* **22,** 1156–1166.

Goddard, J. W. F., J. Tan, and M. Thurai, 1994: Technique for calibration of meteorological radars using differential phase. *Electron. Lett.,* **30,** 166–167.

Gorgucci, E., G. Scarchilli, and V. Chandrasekar, 1994: A robust estimator of rainfall rate using differential reflectivity. *J. Atmos. Oceanic Technol.,* **11,** 586–592.

——, V. Chandrasekar, and G. Scarchilli, 1995: Radar and surface measurement of rainfall during CaPE: 26 July case study. *J. Appl. Meteor.,* **34,** 1570–1577.

——, G. Scarchilli, and V. Chandrasekar, 1996: Operational monitoring of rainfall over the Arno River basin using dual-polarized radar and rain gauges. *J. Appl. Meteor.,* **35,** 1221–1230.

——, ——, and ——, 1999: Specific differential phase estimation in the presence of nonuniform rainfall medium along the path. *J. Atmos. Oceanic Technol.,* **16,** 1690–1697.

Gourley, J. J., and B. E. Vieux, 2005: A method for evaluating the accuracy of quantitative precipitation estimates from a hydrologic modeling perspective. *J. Hydrometeor.,* **6,** 115–133.

——, P. Tabary, and J. Parent du Châtelet, 2006a: Data quality of the Meteo-France C-band polarimetric radar. *J. Atmos. Oceanic Technol.,* **23,** 1340–1356.

——, ——, and ——, 2006b: A fuzzy logic algorithm for the separation of precipitating from nonprecipitating echoes using polarimetric radar observations. *J. Atmos. Oceanic Technol.,* **24,** 1439–1451.

Hagen, M., 2001: On the variation of the parameterization of rainfall rate estimation by dual polarization techniques. Preprints, *30th Conf. on Radar Meteorology,* Munich, Germany, Amer. Meteor., Soc., 644–645.

Hubbert, J., and V. N. Bringi, 1995: An iterative filtering technique for the analysis of copolar differential phase and dual-frequency radar measurements. *J. Atmos. Oceanic Technol.,* **12,** 643–648.

——, V. Chandrasekar, V. N. Bringi, and P. Meischner, 1993: Processing and interpretation of coherent dual-polarized radar measurements. *J. Atmos. Oceanic Technol.,* **10,** 155–164.

Illingworth, A. J., 2003: Improved precipitation rates and data quality by using polarimetric measurements. *Weather Radar: Principles and Advanced Applications,* P. Meischner, Ed., Springer-Verlag, 130–166.

Joss, J., and A. Waldvogel, 1990: Precipitation measurement and hydrology. *Radar in Meteorology: Battan Memorial and 40th Anniversary Radar Meteorology Conference,* D. Atlas, Ed., Amer. Meteor. Soc., 577–579.

——, and R. Lee, 1995: The application of radar–gauge comparisons to operational precipitation profile corrections. *J. Appl. Meteor.,* **34,** 2612–2630.

Keenan, T. D., 2003: Hydrometeor classification with a C-band polarimetric radar. *Aust. Meteor. Mag.,* **52,** 23–31.

——, D. Zrnić, L. Carey, P. May, and S. Rutledge, 1997: Sensitivity of C-band polarimetric variables to propagation and backscatter effects in rain. Preprints, *28th Conf. on Radar Meteorology,* Austin, TX, Amer. Meteor. Soc., 13–14.

——, K. Glasson, F. Cummings, T. S. Bird, R. J. Keeler, and J. Lutz, 1998: The BMRC/NCAR C-band polarimetric (C-POL) radar system. *J. Atmos. Oceanic Technol.,* **15,** 871–886.

Kessinger, C., S. Ellis, J. van Andel, and J. Yee, 2003: The PA clutter mitigation scheme for the WSR-88D. Preprints, *31st Conf. on Radar Meteorology,* Seattle, WA, Amer. Meteor. Soc., 526–529.

Maddox, R. A., J. Zhang, J. J. Gourley, and K. W. Howard, 2002: Weather radar coverage over the contiguous United States. *Wea. Forecasting,* **17,** 927–934.

May, P. T., T. D. Keenan, D. S. Zrnić, L. D. Carey, and S. A. Rutledge, 1999: Polarimetric radar measurements of tropical rain at a 5-cm wavelength. *J. Appl. Meteor.,* **38,** 750–765.

Parent du Châtelet, J., P. Tabary, and M. Guimera, 2005: The PANTHERE Project and the evolution of the French operational radar network and products: Rain-estimation, Doppler winds, and dual-polarization. Preprints, *32d Conf. on Radar Meteorology,* Albuquerque, NM, Amer. Meteor. Soc., 14R.6.

Pellarin, T., G. Delrieu, G.-M. Saulnier, H. Andrieu, B. Vignal, and J.-D. Creutin, 2002: Hydrologic visibility of weather radar systems operating in mountainous regions: Case study for the Ardèche catchment (France). *J. Hydrometeor.,* **3,** 539–555.

Petersen, W. A., and Coauthors, 1999: Mesoscale radar observations of the Fort Collins flash flood of 28 July 1997. *Bull. Amer. Meteor. Soc.,* **80,** 191–216.

Pruppacher, H. R., and K. V. Beard, 1970: A wind tunnel investigation of the internal circulation and shape of water drops falling at terminal velocity in air. *Quart. J. Roy. Meteor. Soc.,* **96,** 247–256.

Ryzhkov, A. V., and D. S. Zrnić, 1995: Comparison of dual-polarization radar estimators of rain. *J. Atmos. Oceanic Technol.,* **12,** 249–256.

——, and ——, 1996: Assessment of rainfall measurement that uses specific differential phase. *J. Appl. Meteor.,* **35,** 2080–2090.

——, and ——, 1998a: Beamwidth effects on the differential phase measurements of rain. *J. Atmos. Oceanic Technol.,* **15,** 624–634.

——, and ——, 1998b: Polarimetric rainfall estimation in the presence of anomalous propagation. *J. Atmos. Oceanic Technol.,* **15,** 1320–1330.

Seliga, T. A., and V. N. Bringi, 1976: Potential use of radar differential reflectivity measurements at orthogonal polarizations for measuring precipitation. *J. Appl. Meteor.,* **15,** 69–76.

——, ——, and H. H. Al-Khatib, 1981: A preliminary study of comparative measurements of rainfall rate using the differential reflectivity radar techniques and a raingage network. *J. Appl. Meteor.,* **20,** 1362–1368.

Szalinska, W., P. Tabary, and H. Andrieu, 2005: Conditional evaluation of convectional versus polarimetric QPE at C-band. Preprints, *32d Conf. on Radar Meteorology,* Albuquerque, NM, Amer. Meteor. Soc., P6R.12.

Tabary, P., 2007: The new French operational radar rainfall product. Part I: Methodology. *Wea. Forecasting,* **22,** 393–408.

Testud, J., 2003: Precipitation measurements from space. *Weather Radar: Principles and Advanced Applications,* P. Meischner, Ed., Springer-Verlag, 199–234.

——, E. Le Bouar, E. Obligis, and M. Ali-Mehenni, 2000: The rain profiling algorithm applied to polarimetric weather radar data. *J. Atmos. Oceanic Technol.,* **17,** 322–356.

Vivekanandan, J., D. N. Yates, and E. A. Brandes, 1999: The influence of terrain on rainfall estimation from radar reflectivity and specific propagation phase observations. *J. Atmos. Oceanic Technol.,* **16,** 837–845.

Young, C. B., B. R. Nelson, A. A. Bradley, J. A. Smith, C. D. Peters-Lidard, A. Kruger, and M. L. Baeck, 1999: An evaluation of NEXRAD precipitation estimates in complex terrain. *J. Geophys. Res.,* **104,** 19 691–19 703.

Zrnić, D. S., and A. V. Ryzhkov, 1996: Advantages of rain measurements using specific differential phase. *J. Atmos. Oceanic Technol.,* **13,** 454–464.

——, and ——, 1999: Polarimetry for weather surveillance radars. *Bull. Amer. Meteor. Soc.,* **80,** 389–406.